Study of the folding and deployment aspects of a Collapsible Rib Tensioned Surface (CRTS) Antenna reflector

Z. You and S. Pellegrino

CUED/D-STRUCT/TR 144

European Space Agency Contract Report.

The work described in this report was done under ESA contract.
Responsibility for its contents resides with the authors or the organisation that prepared it.

ESA Study Manager: W.J. Rits
ESTEC purchase order no 125396

Document no CUED/D-STRUCT/TR 144
Release date 15 March, 1994

ABSTRACT

This report presents the results of a study on the folding and deployment of the CRTS Antenna reflector, a novel concept under development by the European Space Technology Centre (ESTEC). The CRTS reflector consists of three elements: a parabolic membrane, a series of foldable ribs, and an expandable hub.

The present, generic investigation of the folding and deployment properties of the CRTS reflector has focussed mainly on a small scale, symmetric reflector.

The study was divided into two separate phases. The key aims of the first phase were: to identify suitable packaging techniques; to demonstrate their feasibility; and to examine related critical issues, such as the possibility of rib interference during deployment, or possible damage of the membrane. The key aim of the second phase was to obtain an understanding of the deployment process, for a selected packaging technique, in order to analyse the duration of deployment and the stresses induced in the membrane and in the ribs. All of these objectives have been achieved and key results have been validated experimentally.

Three packaging methods for CRTS reflectors have been identified and analysed in detail. Each method is based on a folding pattern whose geometry has been fully worked out and hence can be implemented without difficulty. A trade-off between the three packaging methods has been carried out. Two selected folding schemes have been tested experimentally and a folding apparatus has been developed for the selected packaging scheme, which involves a zig-zag folding of each rib. This scheme is the best in terms of ease of implementation and is joint best in terms of packaging efficiency. A simple folding apparatus has been developed to implement this packaging scheme and, with it, the folding operation has been repeated many times on a 1 m model reflector. Deployment tests have been carried out on the model, packaged in this way.

A detailed experimental investigation of the large displacement, large rotation behaviour of a rib has been carried out, leading to a full characterisation of the moment/rotation relationship of the rib. Numerical investigations of the deployment process have been carried out with the ABAQUS finite element package. Also, an analytical technique has been developed specially for this study. Deployment experiments on small scale ribs with a single fold have proved to be most a valuable tool in assessing the validity of these numerical models.

CONTENTS

1. INTRODUCTION

This report presents the results of a study on the folding and deployment of the Collapsible Rib Tensioned Surface (CRTS) Antenna reflector, a novel concept proposed by W. Rits, of the European Space Technology Centre (ESTEC) [1].

The CRTS reflector consists of three elements: a precision shaped, parabolic *membrane*; a series of thin-walled foldable *ribs* with C-shaped cross-section, arranged in radial directions; and an expandable *hub* supporting the ribs. The hub is contracted during folding/deployment, so that the ribs can deploy the membrane without having to prestress it at the same time. It is then expanded, once the membrane is fully deployed, to apply a state of prestress to the membrane and thus to set it into an accurate shape. A schematic diagram of the reflector is shown in Fig. 1. The membrane consists of identical, flat gores with curved edges, see Fig. 2, taped together. When the reflector is deployed each gore takes a cylindrical shape with parabolic section; hence the overall shape of the reflector is not an exact paraboloid, but only an approximation to it whose accuracy improves as the number of gores is increased. Each rib is held into a pocket formed by the membrane itself, at the seam between two adjacent gores. It is positioned with the convex side facing up, i.e. towards the focus of the reflector. The ribs are attached only to the outer edge of the membrane, and hence can slide relative to the membrane, while remaining inside the pocket, both during folding/deployment of the reflector and also while the membrane is pretensioned.

The present, generic investigation of the folding and deployment properties of the CRTS reflector has focussed mainly on a small scale, symmetric reflector whose properties are given in Table 1. It is believed that the behaviour of this model is representative of full size reflectors, with diameters of 5-10 m and 24-36 ribs. It would have been beyond the scope of the present study to carry out experiments on large physical models and, furthermore, the detailed properties of full-size reflectors are yet to be decided.

The layout of the report is as follows. Section 2 describes the aims of the study. Section 3 presents three different techniques for compactly packaging the reflector; these techniques have been verified on small-scale paper-and-wire models. A simple folding apparatus has been developed for the most promising of the three packaging schemes, and thus the chosen packaging technique has

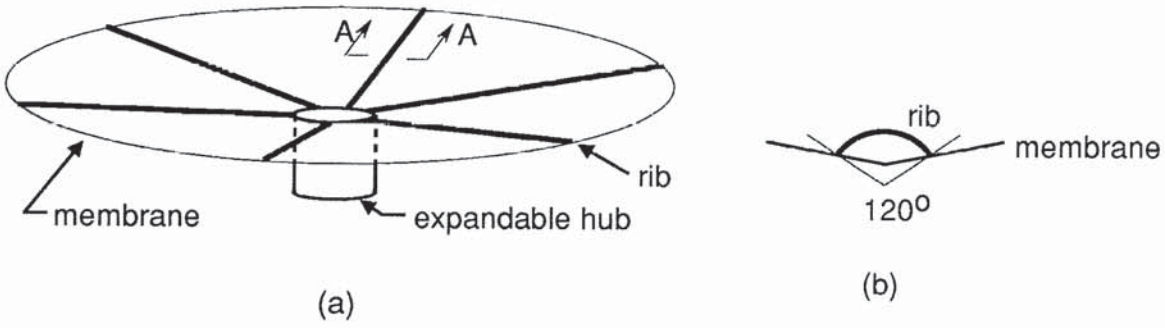

Fig. 1. (a) Schematic view of CRTS reflector. (b) Section A-A.

been verified for the model reflector. Section 4 presents a series of studies that characterise the deployment properties of the CRTS reflector. A deployment experiment on a single rib has been carried out, to measure the large displacement (and large rotation) moment/curvature relationship for the rib. Computational investigations of this deployment problem are presented, including a finite-element analysis with the ABAQUS package and an analytical model specially developed for the type of thin-walled ribs used in the CRTS reflector. Deployment tests have been carried out on the model reflector and are compared to finite-element analyses. Preliminary results have been obtained for a reflector with a diameter of 5.5 m. Section 5 concludes the report.

Table 1. Properties of model reflector.

Reflector	diameter (deployed)	1 m between mid-sides of opposite gores
	focal length	625 mm (hub at 100 mm from front plane)
	hub diameter	100 mm
	no of ribs	6
Membrane	material	Kevlar reinforced Kapton foil
	thickness	0.1 mm
	mass	70 g/m^2
Ribs	material	Copper-Beryllium
	density	$8.4 \cdot 10^3$ kg m^{-3}
	Young's Modulus	$131 \cdot 10^9$ N m^{-2}
	transverse radius of curvature	12 mm
	subtended angle	120°
	thickness	0.1 mm
	length	530 mm

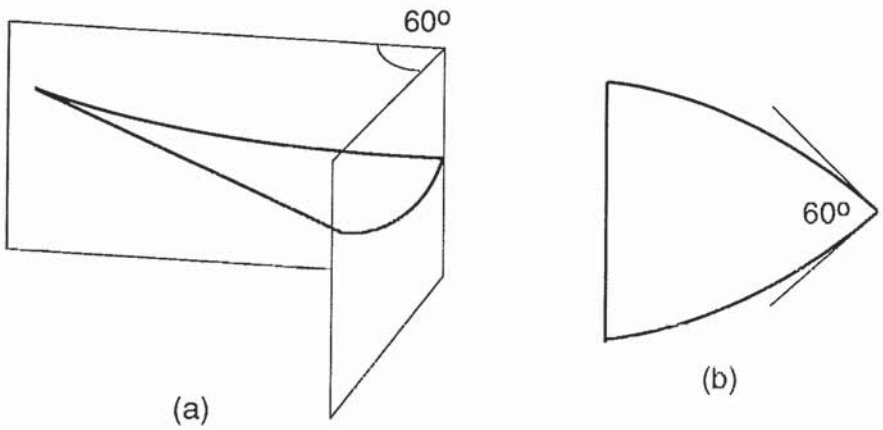

Fig. 2. (a) Perspective view of a single gore. (b) The same gore, in a flat state.

2. AIMS OF THIS STUDY

The detailed aims of this study were set out in the Study Definition Document [2]. The study was divided into two separate phases: Phase (i), review of folding concepts, and Phase (ii), study of deployment aspects.

The key aims of Phase (i) were: to identify suitable packaging techniques; to demonstrate their feasibility; and to examine related critical issues, such as the possibility of rib interference during deployment, possibly resulting in off-nominal deployed geometry, or possible damage of the membrane during deployment or at the end of deployment.

The key aim of Phase (ii) was to obtain an understanding of the deployment process, for a selected packaging technique, in order to analyse the duration of deployment and the stresses induced in the membrane and in the ribs.

3. PACKAGING METHODS

This section presents three different techniques for compactly packaging the membrane of the CRTS reflector. Compact packaging is achieved by minimising the volume of voids in the package. Each packaging technique is based on a fully defined folding pattern, so that the process of packaging and deployment is *repeatable*, can be verified experimentally and can also be simulated by means of suitable computational tools.

Our objective is to package a curved membrane which has positive gaussian curvature [3] along the seams between gores and zero curvature elsewhere. However, a considerable part of our efforts have been directed towards flat membranes: the first two packaging schemes have been developed for flat membranes and have turned out to work well for curved membranes as well, while the third scheme has been obtained by extending an already known packaging scheme for flat membranes.

3.1 General properties of folding patterns

Let us consider the flat, thin membrane shown in Fig. 3, with four straight folds meeting at a common point. The sum of the angles α_1, α_2, α_3, α_4 must be 360° because the membrane can be made absolutely flat, i.e. its angular defect [3] at point O is zero. Thus

$$\alpha_1 + \alpha_2 + \alpha_3 + \alpha_4 = 360° \qquad (1)$$

For the membrane to fold compactly, see Fig. 3(b), the difference between two adjacent angles has to be equal to the difference between the other two angles, hence

$$\alpha_4 - \alpha_1 = \alpha_3 - \alpha_2$$

and, re-arranging

$$\alpha_1 + \alpha_3 = \alpha_2 + \alpha_4 \qquad (2)$$

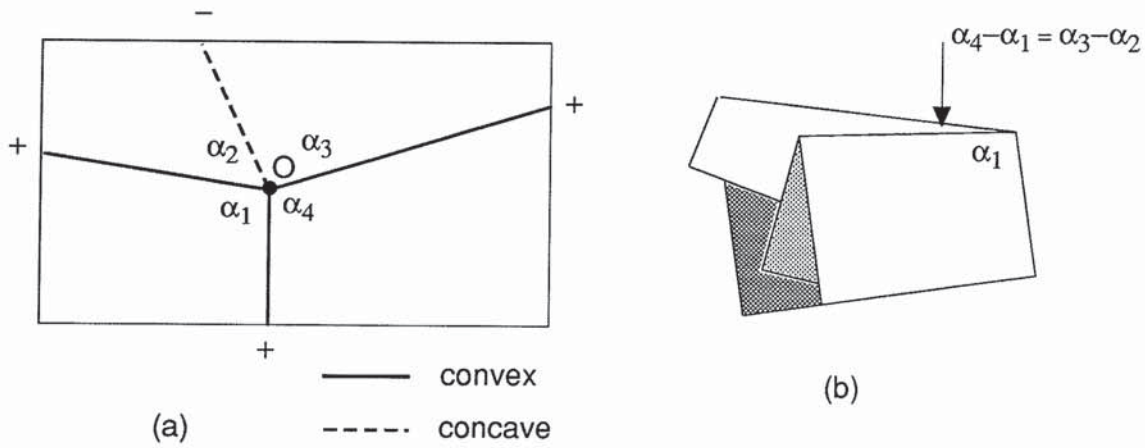

Fig. 3. Flat membrane with four folds meeting at point O.

Equations 1 and 2 can be generalised to folding patterns with more than four fold lines meeting at a point, but note that four is the minimum number of folds that must intersect, in general, for the membrane to fold. There is only one trivial exception, when two folds are collinear. Also note that the folds in Fig. 3 are straight: curved fold lines would require that the membrane bends out of plane while it is folded and, apart from the complexity of this analysis, the packaged configuration would not be compact.

In Fig. 3(a) there are *three convex folds*, where the membrane folds downwards, denoted by solid lines, and a *single concave fold* line, denoted by a broken line. This drawing convention will be followed throughout this report.

The general sign rule that has to be satisfied at any point of intersection of four fold lines is that one fold should be of sign opposite to the other three [4]. Similar conditions apply if more than four folds meet at a point.

Next, we present a simple, symmetric folding pattern to roll up a flat, six-gore membrane into a package of toroidal shape. The packaging scheme is shown in Fig. 4, for a 60° sector. Figure 4(a) is a perspective view of the membrane, shown flat, while Fig. 4(b) shows the rolled up configuration. To preserve six-fold rotational symmetry about the centre O throughout folding, the edges of this sector can move only within vertical radial planes forming an angle of 60°. Hence, corresponding points on opposite sides of the sector have to move closer — in the hoop direction — while the membrane is rolled up towards the centre.

The general fold pattern behind this packaging scheme is shown in Fig. 5. It is based on three radial fold lines, two along the edges of the sector and one in the middle, with alternate concave and convex folds. The radial folds are joined by a series of transverse concave folds. Thus, the sector is divided into a set of quadrangles and two triangles, near the centre. This pattern is fully defined by the lengths $\overline{OP}$, $\overline{PQ}$, $\overline{QR}$, etc. (or by the lengths $\overline{OA}$, $\overline{AB}$, $\overline{BC}$, etc.) and by the angles α_1 and α_2, β_1 and β_2, etc. The complete fold pattern is obtained from the folding pattern shown in Fig. 5(a), by symmetry. Hence, there are four fold lines meeting at all points other than O, of which

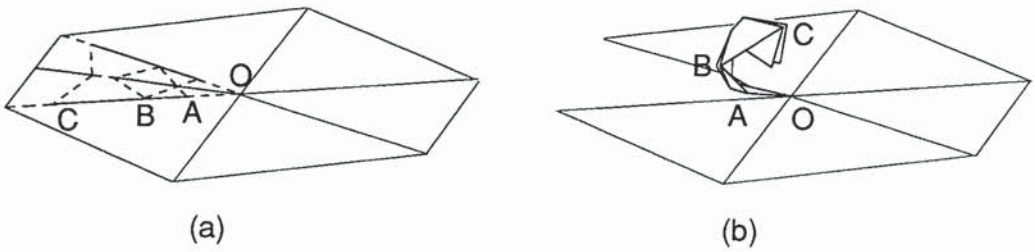

Fig. 4. Rotationally symmetric folding scheme to roll up a gore.

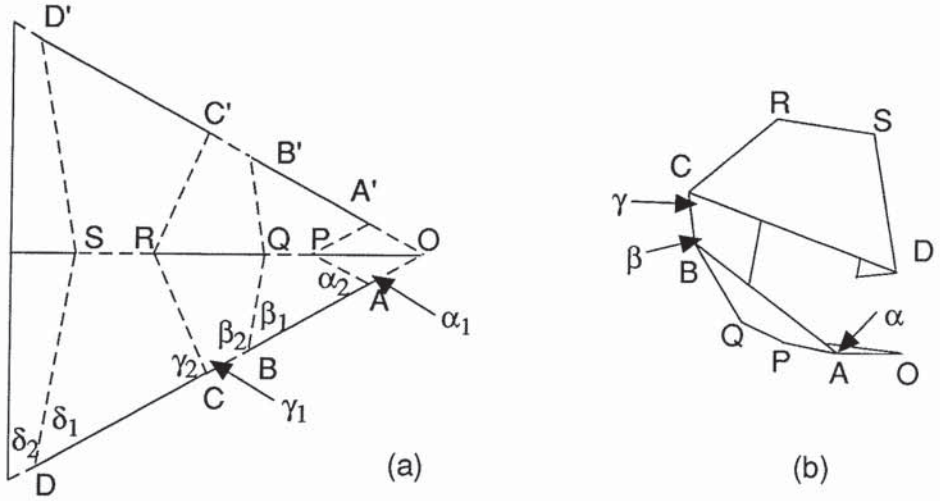

Fig. 5. (a) Detailed fold pattern for a single gore. (b) The same gore, flattened.

three folds are concave and one is convex, thus satisfying the above sign rule. The number of fold lines at O is twelve.

Only some combinations of the above geometric parameters correspond to acceptable folding patterns, as can be easily verified by making a few paper models and attempting to fold them. Most folding patterns will produce non-compact packaged configurations or cannot even be packaged completely because of interference between different panels.

Next, we describe a systematic procedure to choose values for the geometric parameters of the fold pattern while avoiding these difficulties. First, we choose values for all angular parameters by identifying all analytical conditions that must be satisfied by the angles between folds meeting at a single point and, if these conditions do not identify a unique set of values, we choose the particular solution that is easiest to implement in practice.

Because we are dealing with a flat membrane

$$\alpha_1 + \alpha_2 = \beta_1 + \beta_2 = \ldots = 180° \tag{3}$$

Also, considering the membrane flat, in a vertical plane as shown in Fig. 5(b), we can define the following angles

$$\alpha = O\hat{A}P - P\hat{A}B = \alpha_1 - \alpha_2$$
$$\beta = C\hat{B}Q - Q\hat{B}A = \beta_2 - \beta_1 \qquad (4)$$
etc.

These angles govern the shape of the folded membrane. Actually, this flat configuration cannot be reached by the complete membrane, because the edges of each sector must lie in radial planes forming an angle of 60°, and hence cannot become coplanar.

To avoid that side OA interferes with AB and, similarly, that AB interferes with BC, etc. during folding, all of these angles must be non-negative, hence

$$\alpha = \alpha_1 - \alpha_2 \geq 0$$
$$\beta = \beta_2 - \beta_1 \geq 0 \qquad (5)$$
etc.

To reduce the volume of the stowed membrane, these angles should be as small as possible. Indeed, in Scheme 1, in the next section, they will all be set equal to zero.

After setting the values of all angular parameters, the shortest possible length parameters are chosen, for maximum packaging efficiency. For example, in Fig. 5(b) QP could be made a bit shorter and, indeed, even $\overline{QP} = 0$ would be acceptable.

3.2 Scheme 1

Figure 6 shows a packaging scheme for a flat membrane with a rigid hub. This scheme is based on Fig. 5 but a rigid, triangular element OAA' has been included at the centre. The membrane folds along the edge of this rigid element, i.e. along the concave fold AA'. Two further concave folds join A and A' to point P, see Fig. 5(a), where the earlier folding pattern begins. To achieve a compact package, folds PQ and BC have been shrunk to a single point in Fig. 6, and hence points B and C, and P and Q coincide. Thus, the folding pattern consists mainly of triangles, instead of quadrangles, and the number of folds meeting at a common point increases accordingly.

The equations written in the previous section have to be modified. For example, there are now six fold lines meeting at point B, allowing for the two fold lines that belong to the sector adjacent to that shown in Fig. 6(c). Equation 3 becomes

$$\alpha_1 + \alpha_2 + \alpha_3 = \beta_1 + \beta_2 + \beta_3 = 180° \qquad (6)$$

and Eq. 4 becomes

$$\beta = -\beta_1 + \beta_2 - \beta_3 \qquad (7)$$

At point A the situation is rather different. When the membrane is fully folded, the hub element OAA' lies in a horizontal plane, while the membrane element AQB lies in a vertical plane. The treatment of Section 3.1, which is valid if all elements with a common point lie in the

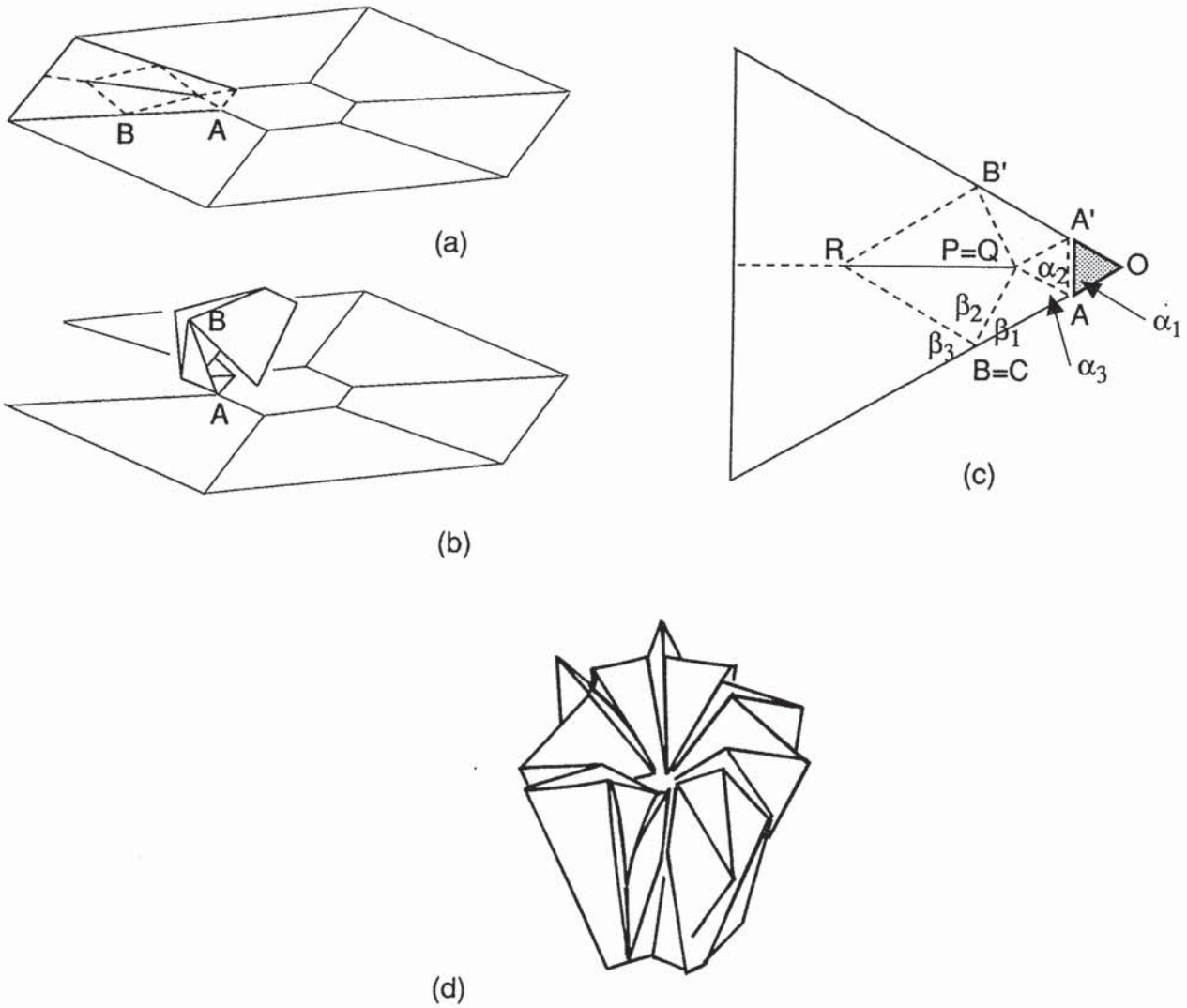

Fig. 6. Folding Scheme 1: (a,b) perspective views, (c) plan view, (d) perspective view of packaged membrane.

same plane when they are folded, is not applicable here. This difficulty can be resolved by noting that OAA' can become orthogonal to AQB if AA'Q can fold over OAA'. This requires that

$$\alpha_2 = \alpha_1 = 60° \tag{8}$$

Substituting these values into Eq. 6 gives $\alpha_3 = 60°$. To calculate the next set of angles we choose $\beta = 0$ for compactness. Equations 6-7 yield

$$\begin{cases} \beta_2 = 90° \\ \beta_1 + \beta_3 = 90° \end{cases} \tag{9}$$

The simplest solution has $\beta_1 = 30°$ and $\beta_3 = 60°$, for which folds BR and AQ are parallel.

Figure 6(d) is a sketch of a card model of a six gore, curved membrane with a (deployed) diameter of 360 mm. In this model the centre dip is 80 mm, corresponding to a reflector with focal length to

diameter ratio of 0.281. This value is much smaller than the CRTS reflector, but has been chosen to verify that the packaging scheme works for a highly curved membrane, even though it has been derived for flat membranes. The figure shows that the folding scheme works well for this model.

A computational test of the folding process was carried out, to simulate the complete folding sequence of a single gore and hence verify that no strains are induced in the membrane by this packaging scheme. The gore was modelled as an assembly of rigid triangular plates of zero thickness, connected by revolute joints along the edges. The edge nodes were constrained to lie in two fixed radial planes throughout the simulation. In the initial configuration all nodes were set to lie on a cylindrical surface. The expected, rolled-up configuration was obtained by deploying the single mechanism of this assembly within an iterative computational scheme.

3.3 Scheme 2

Figure 7 shows a different packaging scheme, also valid for a membrane with a rigid hub. Like Scheme 1, it is based on a fold pattern with radial folds joined by transverse folds, but here the transverse folds are alternately convex and concave, so that the membrane folds into a concertina, instead of rolling up. During the folding process the edge points B, D and B', D' move up, while points C and C' move down relative to the fixed hub.

The calculation of the angles defining the fold pattern follows similar lines to the previous section. We take $\alpha_2 = \alpha_3 = 60°$, so that AA'Q can fold over OAA', as explained for Scheme 1. At B we choose $\beta = 0$ and hence, as in Scheme 2

$$\beta_1 = 30°, \beta_2 = 90°, \text{ and } \beta_3 = 60° \tag{10}$$

At C we choose $\gamma = 0$ and hence from Eqs 3-4

$$\begin{cases} \gamma_1 + \gamma_2 = 180° \\ \gamma = \gamma_1 - \gamma_2 = 0 \end{cases} \tag{11}$$

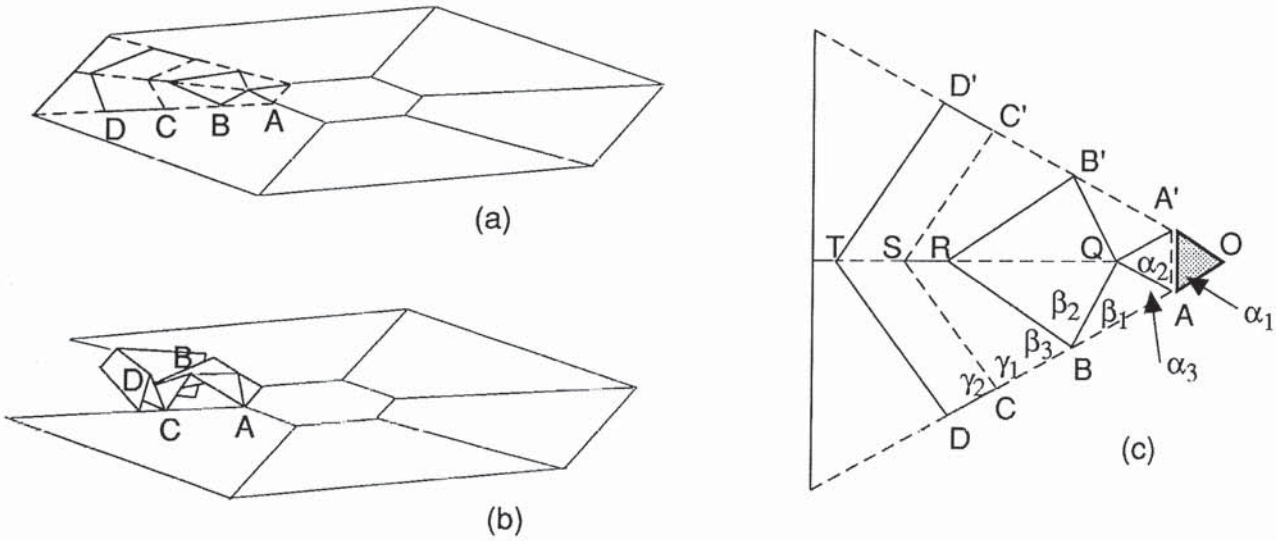

Fig. 7. Folding Scheme 2: (a,b) perspective views, (c) plan view.

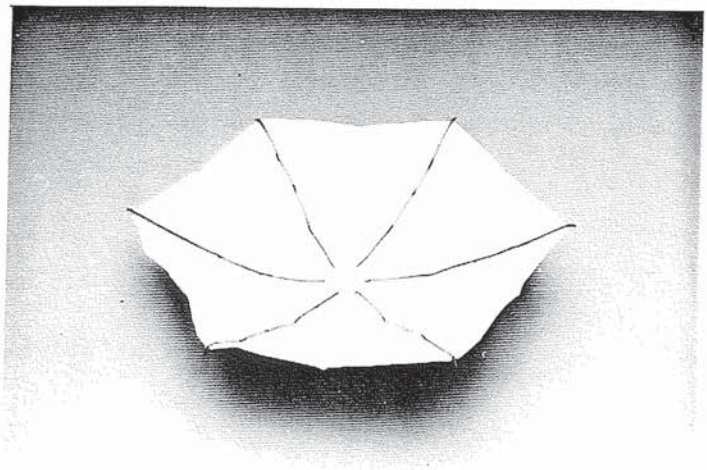

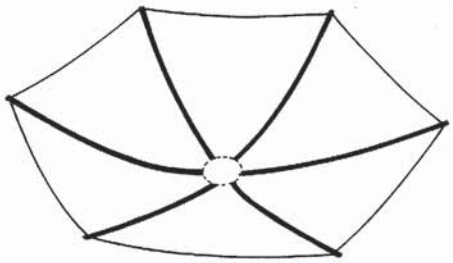

(a)

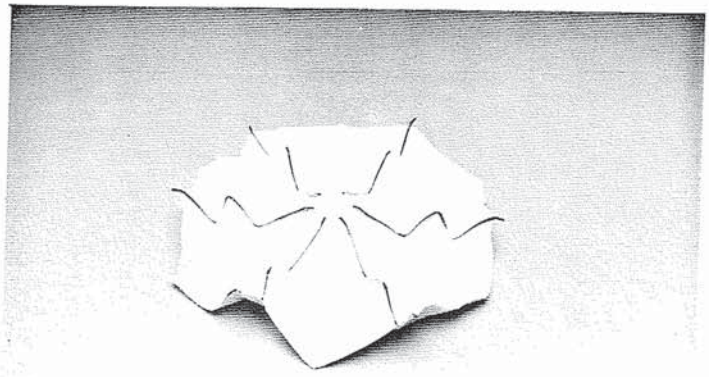

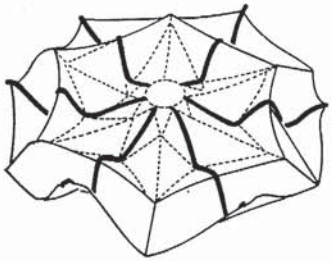

(b)

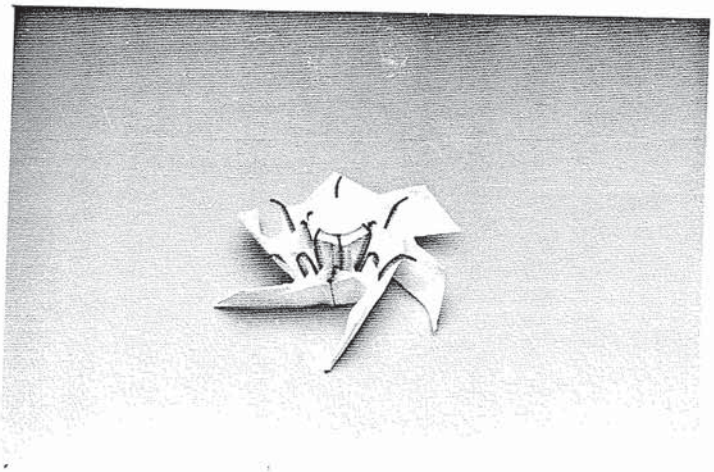

(c)

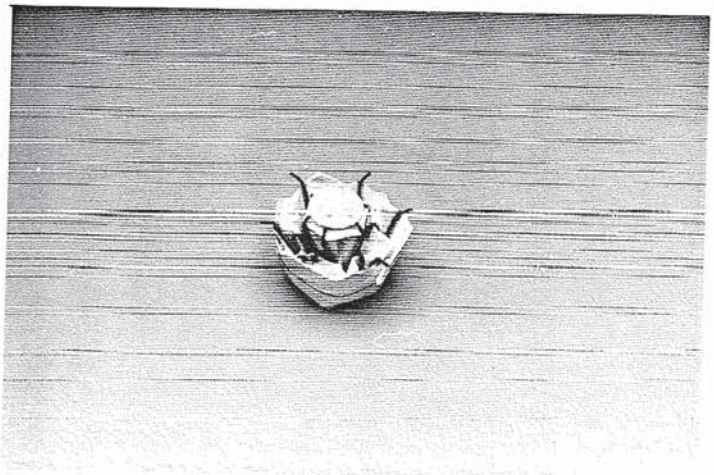

(d)

Fig. 8

yielding

$$\gamma_1 = \gamma_2 = 90° \tag{12}$$

The packaging scheme is illustrated in Fig. 8, which shows a series of photographs of a simple paper-and-wire model and drawings traced from the photographs. Figure 8(a) shows the curved membrane, fully deployed and supported by six curved ribs. The membrane has the same geometric properties of the model described in Section 3.2. Figure 8(b) shows the model partially packaged, with four folds in each rib. Note that the first fold is right at the edge of the hub, as required by the folding pattern. The ribs are fully folded in Fig. 8(c) and finally, in Fig. 8(d), the outer part of the membrane is wrapped around the package.

This packaging scheme is quite intuitive; each rib is folded alternately up and down, in a zig-zag shape, and the membrane is packaged between the ribs, in a way that is compatible with the folding of the ribs. Figure 9 shows a section through two opposite ribs, with four equidistant folds. The membrane is not shown. With reference to Fig. 7(c), here we have chosen $\overline{QR} = \overline{TS}$, and $\overline{RS} = 0$. The diameter and height of the packaged membrane can be changed quite freely, simply by altering the number of folds and the distance between them, respectively.

Thin-walled ribs fold naturally at a radius r, equal to their transverse radius of curvature, see also Section 4.2. Therefore, the diameter D of the packaged membrane is approximately equal to the hub diameter 2R plus 2r times the total number n of folds in a rib

$$D \cong 2R + 2nr \tag{13}$$

The package height H is approximately equal to the rib length L divided by the number of folds

$$H \cong \frac{L}{n} \tag{14}$$

In Fig. 9 there are four folds in each rib, hence $n = 4$. The above equations neglect the arc length of the folds.

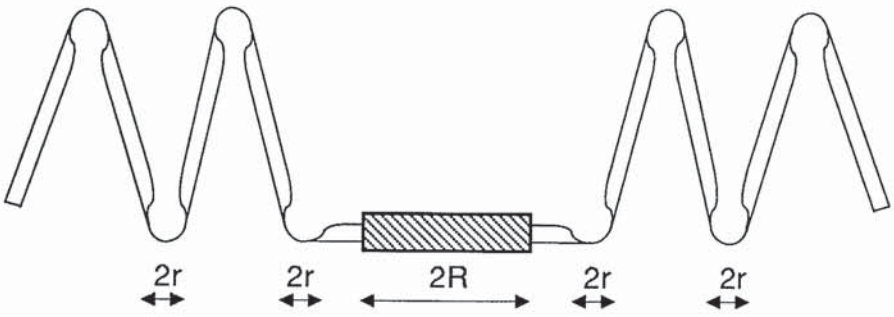

Fig. 9. Cross section through two opposite ribs (folded) and the hub.

3.4 Scheme 3

The third packaging scheme is quite different from the previous two. The idea is to wrap the membrane and the ribs around the hub, rather than to fold them radially. This approach is based on a packaging technique that was first developed for (flat) solar sails [5]. Because the CRTS membrane is not flat, a suitable pre-folding technique will be introduced, to flatten the membrane before it is wrapped. For clarity the two phases of the folding operation are presented separately, in the next two sections.

3.4.1 Pre-folding. The pre-folding scheme is quite complex and is best introduced by a simpler, preliminary example. Figure 10(a) shows a curved membrane consisting of six flat gores; Fig. 10(a.i) is a perspective view, while Fig. 10(a.ii) is a top view. This membrane is identical to the membrane of Fig. 1, but it is not attached to a rigid hub and hence there are no constraints on the folding of its inner edge.

This membrane can be flattened by transforming the curved edges of each gore into straight edges with an enclosed angle of 60°. In Fig. 10(b.i) a straight fold at an angle of 30° to the axis has been formed into a gore (30° is half the angle subtended by the gore) thus dividing the gore into two parts, A and B. In Fig. 10(b.ii) part B has been folded over part A to obtain a gore with a straight edge. The flat membrane shown in Fig. 10(b.iii) has been obtained by carrying out the same operation simultaneously for all six gores making up the continuous membrane.

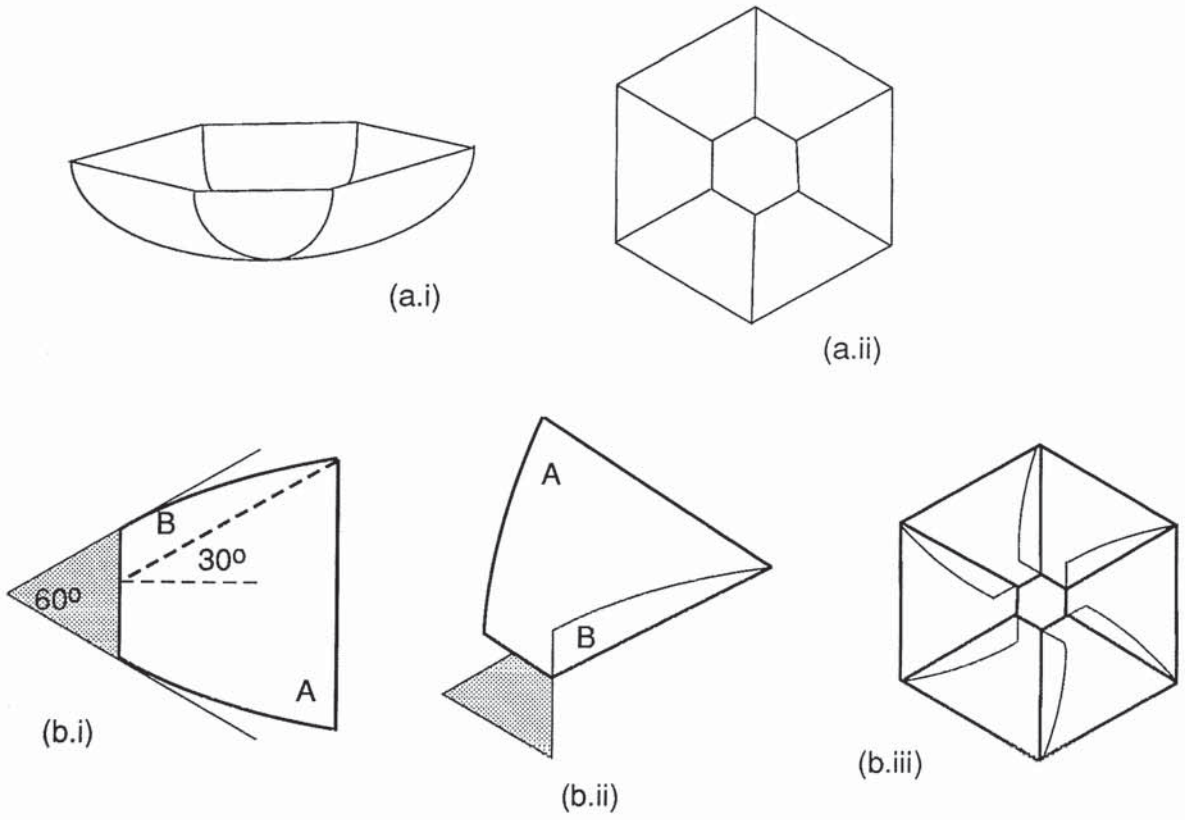

Fig. 10. (a) Curved and (b) flattened membrane.

This type of pre-folding has the effect of reducing the perimeter of the inner edge of the membrane, hence the inner perimeter in Fig. 10(a.ii) is greater than in Fig. 10(b.iii). In the CRTS reflector it is unlikely that such a reduction can be achieved by contracting the hub. Furthermore, the folding of part B of each gore over part A requires the inner edge of the membrane not to be continuously attached to the hub, which would have undesirable effects on electrical performance.

All of these problems are resolved if a more elaborate type of pre-folding is adopted, see Fig. 11. Here the membrane is flattened in a plane parallel to the hub, a small distance above it, by forming two parallel, concave folds AA' and BB' in each gore, Fig. 11(a). Then, AA'C'C is folded perpendicularly to the hub, and BB'C'C is folded perpendicularly to AA'B'A, hence now BB'C'C lies in a plane above the hub, Fig. 11(b). Next, point D is introduced along BB'; two further folds are formed, DE and AD; and the sign of the rotation along BD is reversed. DE is a convex fold, i.e. concave if seen from the top, Fig. 11(b). It divides BB'C'C into two parts, analogous to parts A and B in Fig. 10. AD is also a convex fold, and it is required to increase to four the number of folds intersecting at point D, thus satisfying the condition stated in Section 3.1. Finally, DBCE is folded over DB'C'E, Fig. 11(c). This final configuration is analogous to Fig. 10(b.ii), but now most of the membrane lies in a plane above the hub. The complete fold pattern for a single gore is shown in Fig. 11(d), while a perspective view of the folding process is shown in Fig. 12.

The above process can be carried out on the six gores simultaneously, thus flattening the whole membrane, as shown in Fig. 13. Note that the hub is completely hidden in Fig. 13(a).

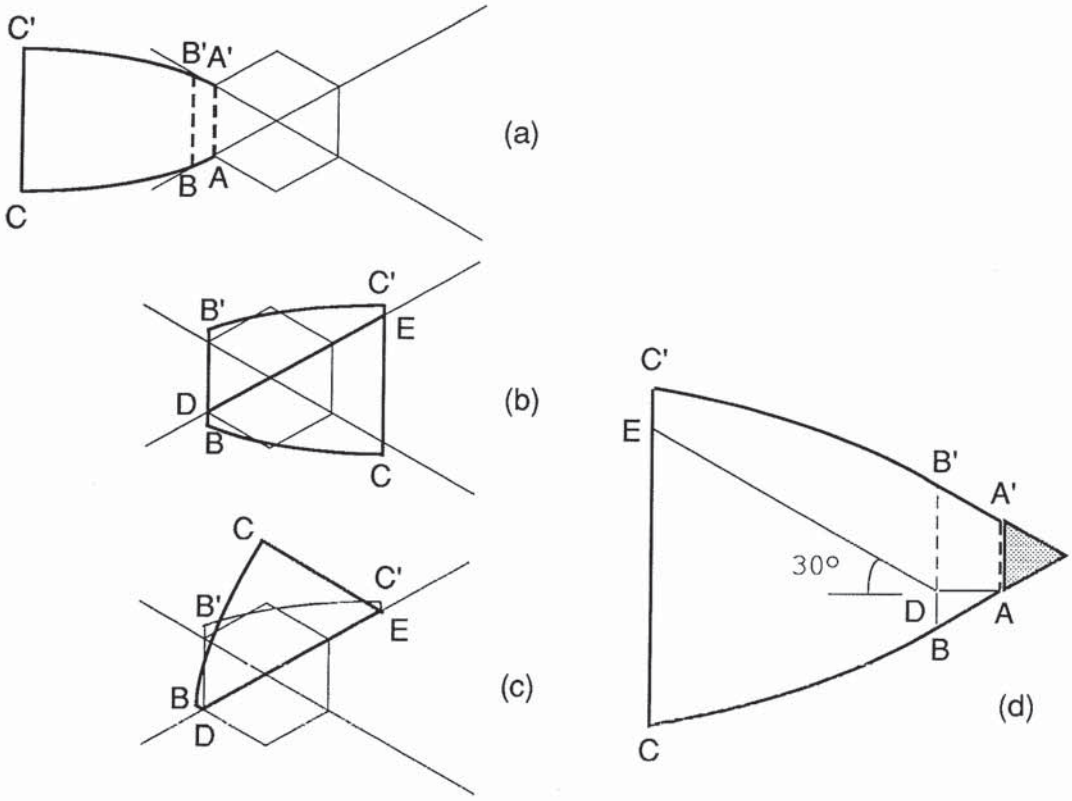

Fig. 11. Folding scheme to flatten a curved membrane connected to a rigid hub. (a-c) Top view of pre-folding sequence for a single gore. (d) Plan view of fold pattern.

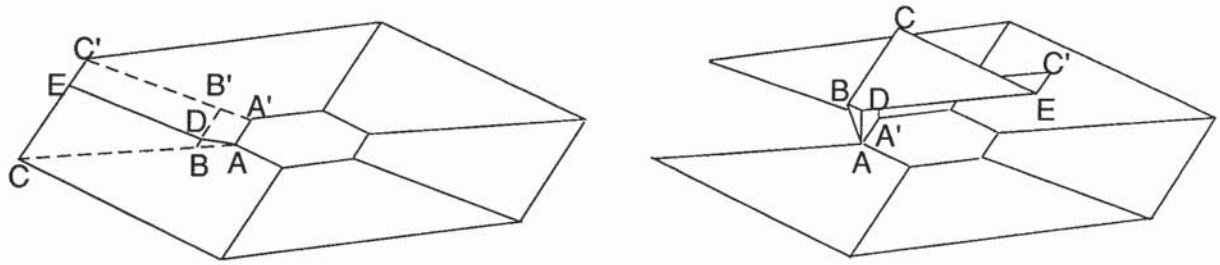

Fig. 12. Perspective views of pre-folding of a gore.

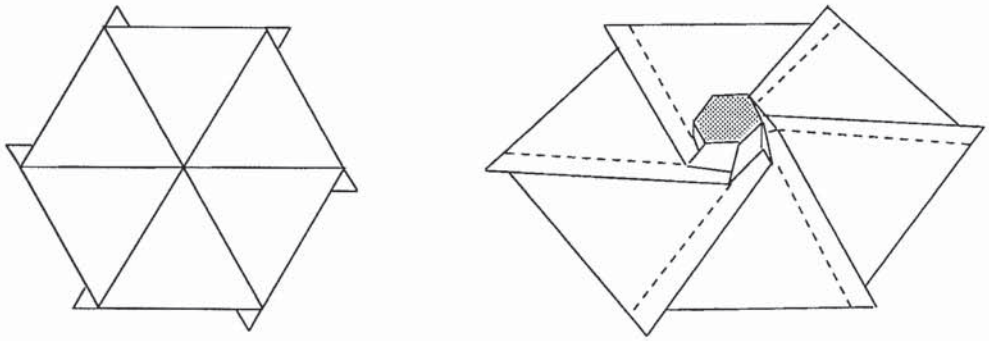

Fig. 13. (a) Top view and (b) bottom view of membrane, after pre-folding.

3.4.2 Wrapping. The folding pattern for wrapping a membrane of negligible thickness around a hexagonal hub whose circumscribed circle has a radius R' (R' > R) is shown in Fig. 14. It is shown in [5] that $\beta = 30°$, $\delta = 90°$, the a-folds are collinear, and the b-folds are parallel and equidistant.

The folding pattern for a membrane of small thickness t is not much different from Fig. 14, but the above simple results are no longer true. All fold lengths and fold angles have to be calculated allowing for the thickness of the membrane. The coordinates of the points of intersection between the fold lines are considered, both in the fully packaged configuration and in the flat configuration. Basically, the aim of the calculation is to find the shape of a "master" a-fold, e.g. P_{11}, P_{12}, P_{13} in Fig. 15(a), from which the other five a-folds can be obtained by symmetry.

Figures 15(b, c) are top views of the first a-fold when the membrane is fully packaged. Let this fold be convex. The cylindrical coordinates in the system O, r, θ, z, see Fig. 15(a), of the points that define this fold are

$$P_{11} = \begin{pmatrix} R' \\ 0 \\ 0 \end{pmatrix}, \quad P_{12} = \begin{pmatrix} R'+u \\ 60° \\ z_2 \end{pmatrix}, \quad P_{13} = \begin{pmatrix} R'+2u \\ 120° \\ z_3 \end{pmatrix}, \quad \text{etc.} \tag{15}$$

where z_2, z_3, etc. are positive quantities to be determined, and

$$u = \frac{t}{\cos 30°} \tag{16}$$

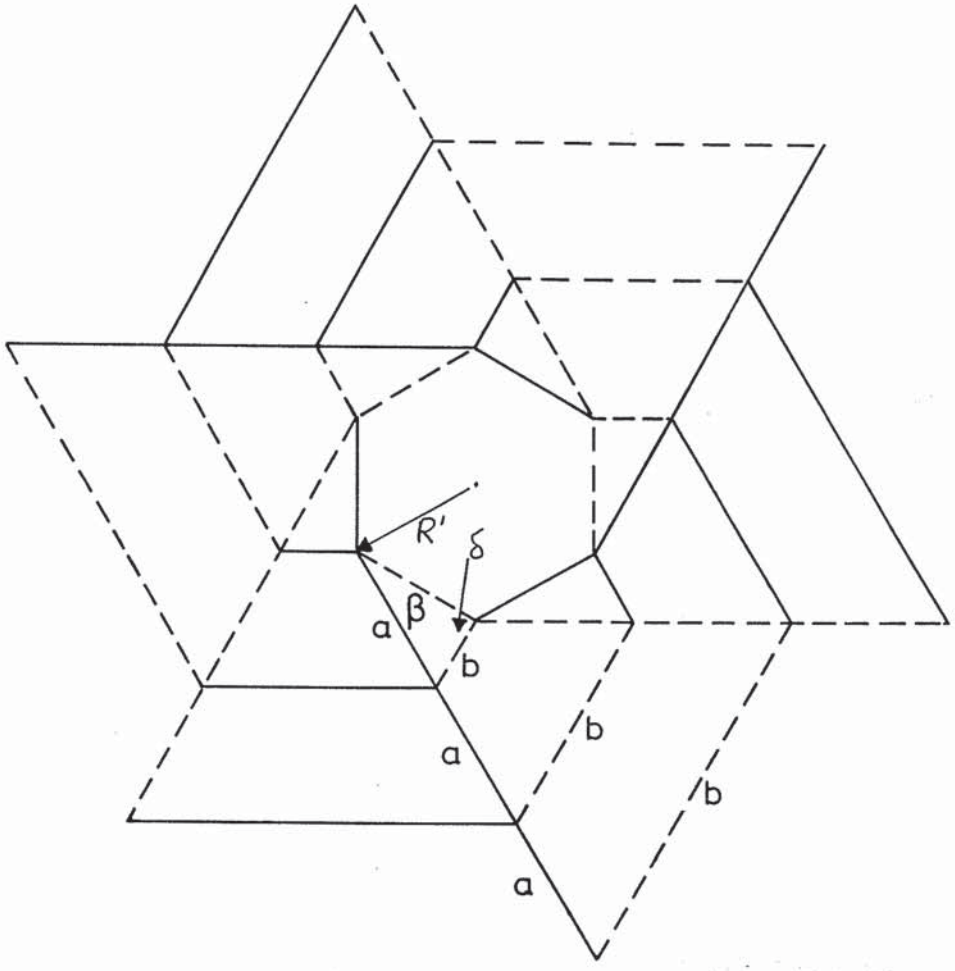

Fig. 14. Folding pattern to wrap a membrane of zero thickness around a hexagonal hub.

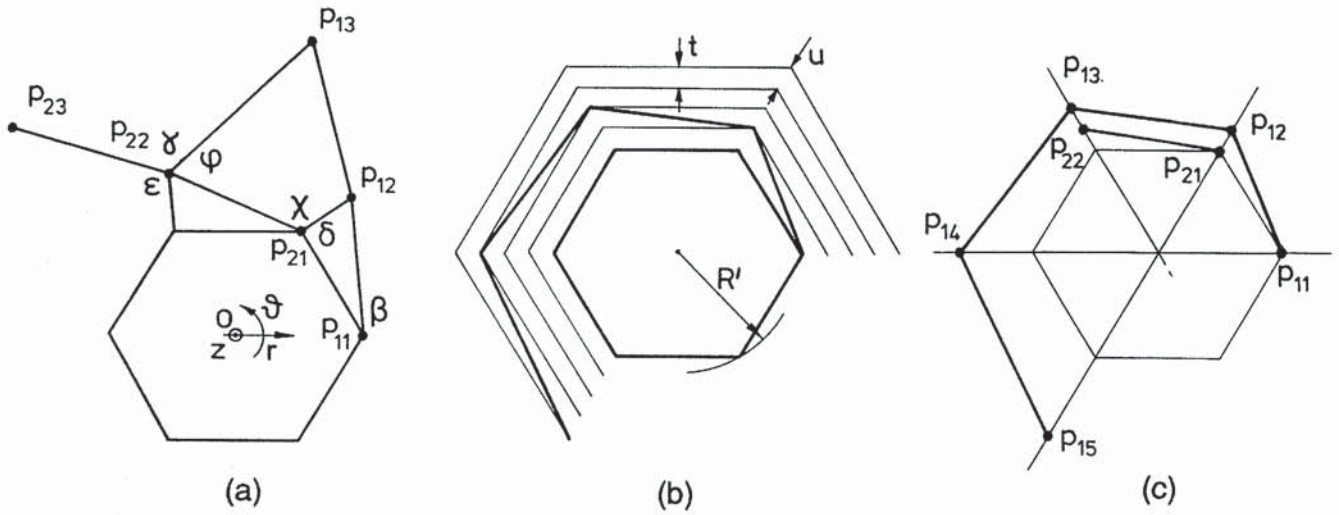

Fig. 15. Folding pattern to wrap a membrane of thickness t. (a) Plan view. (b, c) Top views of first a-fold, after wrapping.

The points that define the second fold, which is concave, are

$$P_{21} = \begin{pmatrix} R' \\ 60° \\ 0 \end{pmatrix}, \quad P_{22} = \begin{pmatrix} R'+u \\ 120° \\ -z_2 \end{pmatrix}, \quad P_{23} = \begin{pmatrix} R'+2u \\ 180° \\ -z_3 \end{pmatrix}, \quad \text{etc.} \tag{17}$$

Note that, for simplicity, the thickness of the hub has been neglected and hence the z-coordinates of all vertices P_{i1}'s vanish. Also, by symmetry, the z-coordinates of equal numbered vertices on different folds are equal in absolute value.

To calculate the z-coordinates of the points that are not part of the hub, we write an equation equivalent to Eq. 1 for each point that defines the first a-fold. For example, for point P_{11} (or P_{21}) the equation is

$$120° + \beta + \chi + \delta = 360° \tag{18}$$

The direction cosines of the angles β, χ, δ are calculated by taking the dot-products of unit vectors between suitably chosen vertices, in the wrapped configuration. Hence

$$\beta = \arccos\left(\frac{(P_{12} - P_{11})}{\|P_{12} - P_{11}\|} \cdot \frac{(P_{21} - P_{11})}{\|P_{21} - P_{11}\|} \right) \tag{19}$$

$$\chi = \arccos\left(\frac{(P_{22} - P_{21})}{\|P_{22} - P_{21}\|} \cdot \frac{(P_{12} - P_{21})}{\|P_{12} - P_{21}\|} \right) \tag{20}$$

$$\delta = \arccos\left(\frac{(P_{21} - P_{11})}{\|P_{21} - P_{11}\|} \cdot \frac{(P_{12} - P_{21})}{\|P_{12} - P_{21}\|} \right) \tag{21}$$

These dot-products can easily be taken after converting the cylindrical coordinates of the relevant vertices to a Cartesian system with the same origin O. Then, these expressions are substituted into Eq. 18, which is solved for the unknown z_2. Finally, β and χ are calculated from Eqs 20-21.

Next, to calculate z_3 and hence ε, ϕ, see Fig. 15(a), the angles ε, ϕ and γ are expressed in terms of the coordinates of points P_{11}, P_{12}, P_{21}, P_{22}, and P_{31} by equations analogous to (19-21) and then substituted into

$$\varepsilon + (180° - \beta - \delta) + \phi + \gamma = 360° \tag{22}$$

which is equivalent to Eq. 1.

This approach can be extended until a sufficient number of points on the master a-fold have been determined, from which the complete folding pattern is obtained. Similar folding patterns can be obtained for any polygonal hub with an even number of sides, see Fig. 16.

The same approach works well for a curved membrane which has been flattened by pre-folding, as

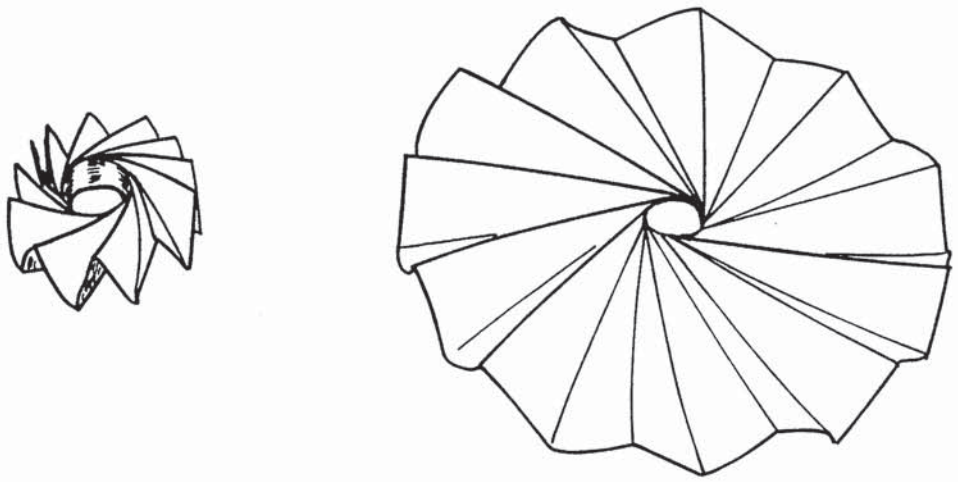

Fig. 16. Wrapping of a flat membrane around a 24-sided hub.

discussed in Section 3.4.1. Figure 17 shows a series of photographs, and line diagrams traced from the photographs, of a paper-and-wire model similar to that described in Section 3.3. Figure 17(a) is a bottom view of the flattened membrane, to be wrapped around a hub whose radius R' is about 50% greater than R, the actual hub radius. The ratio R'/R could be significantly smaller in a bigger model. Figure 17(b) illustrates the wrapping process. Figures 17(c-d) are a top view and a side view of the final package. In the calculation of the folding pattern for wrapping this model, the thickness t was taken to be 2 mm, to allow for the thickness increase caused by pre-folding.

If the number of a-folds is equal to the number of ribs m, the pre-folding presented in Section 3.4.1 brings the edges between gores, and hence the ribs of the CRTS reflector, approximately along the a-folds of the folding pattern for wrapping, as can be seen in Fig. 17. An alternative would be to arrange the wrapping pattern so that the ribs are located half-way between the a-folds, and hence wrap in the plane of the hub. Note that the number of a-folds need not be equal to m. For example, a larger value could be chosen, to reduce the package height. However, arrangements where the ribs cross the a-folds should be avoided. They require localised folds in the ribs similar to those in Schemes 1 and 2, which would increase both the diameter of the package and the complexity of the packaging operation.

The package size can be predicted quite easily and, for example, if the number of a-folds is equal to the number of ribs m, the package height is

$$H \cong 2L\sin\frac{180}{m} - R\tan\frac{180}{m} \tag{23}$$

while the minimum package diameter is

$$D \cong 2R' + \frac{L - R - R'}{2\pi R'}t \tag{24}$$

where $$R' \geq R\left(1 + \sin\frac{180}{m}\tan\frac{180}{m}\right).$$

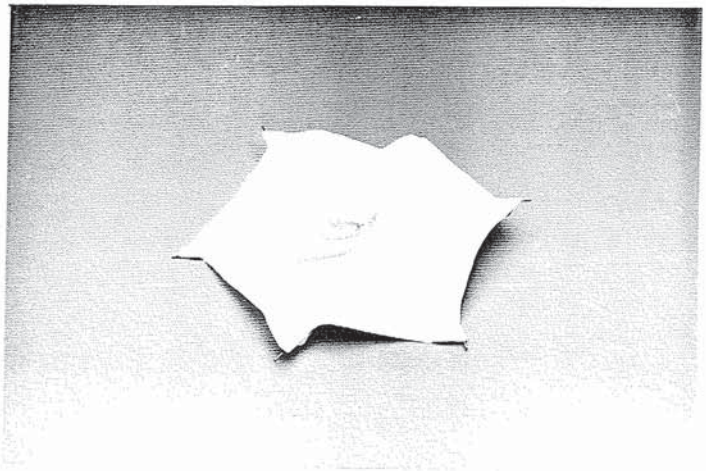

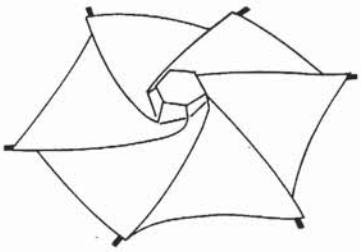

(a)

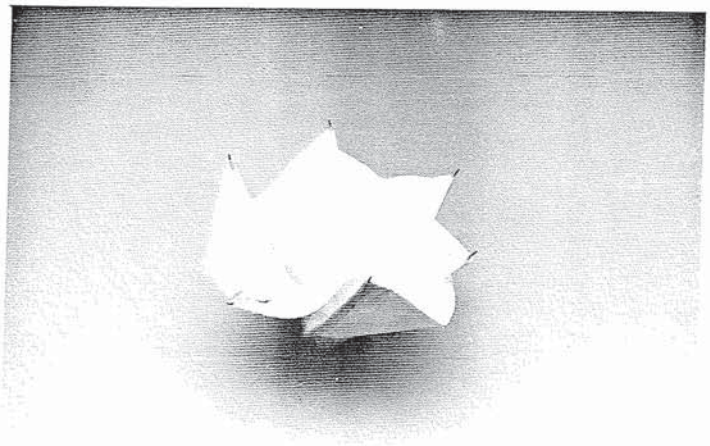

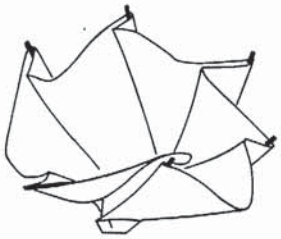

(b)

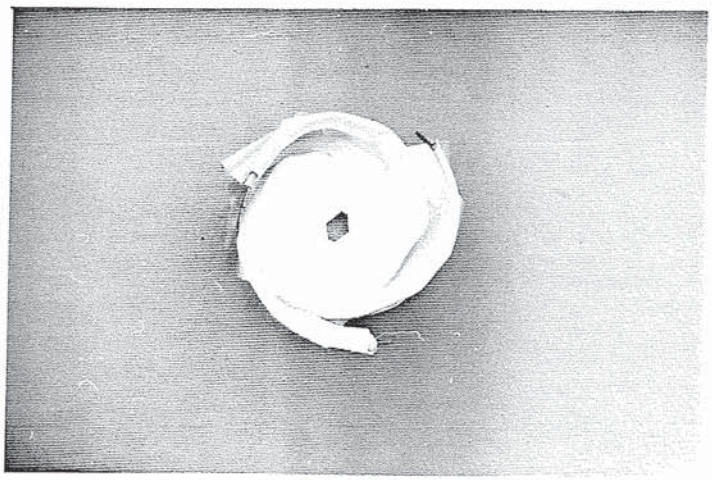

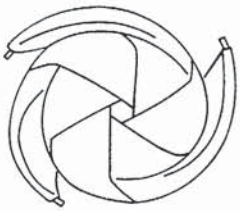

(c)

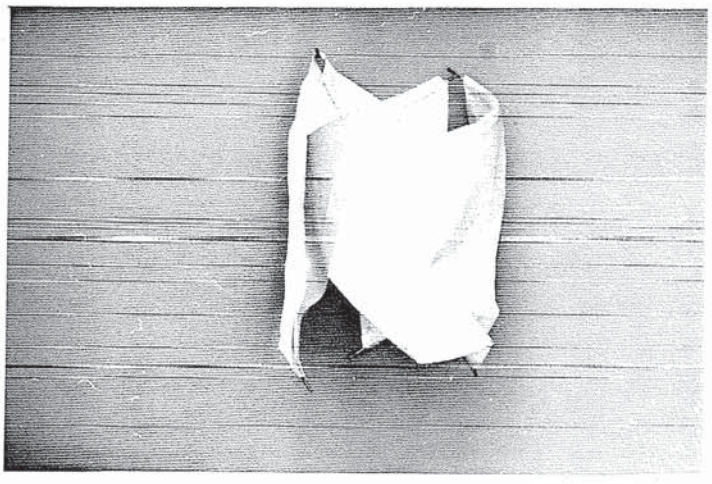

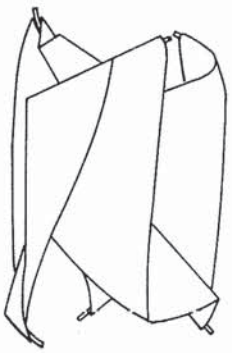

(d)

Fig. 17

3.5 Comparison of three packaging methods

A trade-off between the three packaging methods has shown that Scheme 2 is the most promising. The trade-off was based on (i) packaging efficiency, (ii) complexity of the folding process, and (iii) the possibility that the reflector might deploy into an off-nominal configuration.

(i) In terms of *packaging efficiency*, Schemes 2 and 3 are the best because they minimise the volume of gaps in the package. Scheme 2 is more flexible, because the height and diameter of the package can be readily modified to suit mission requirements. In Scheme 3 some space is taken by the region where the ribs bend and twist, near the hub, but after that the ribs wrap nicely around the package. With this scheme, though, changing the size of the package requires a careful re-analysis of the whole packaging scheme.

(ii) In terms of *complexity* of the folding process, Scheme 2 is the best and its practical implementation has been tested by experiment, see Section 3.6. It is expected that implementing Scheme 1 should also be relatively straightforward, even though it may be difficult to ensure that the rib folds remain in the required positions, after packaging. The implementation of Scheme 3 appears to be rather complex, but has yet to be investigated in detail.

(iii) Quantitative estimates of the possibility that the reflector might *deploy into a non-nominal configuration* would be well beyond the time scale and resources available for this pilot study, but the following preliminary considerations should be a useful guide for further work.

In Scheme 1 there is the possibility that the tip segments of two or more ribs might become interlocked during deployment, because all ribs are bent towards the centre of the hub in the packaged configuration, and they tend to move over centre during deployment. For this reason, this scheme was abandoned.

In Scheme 2 two potentially critical aspects were considered. First, a rib with several up-and-down folds is an unstable, energy loaded system that needs to be suitably restrained to prevent it from, e.g., buckling out of plane within the volume of the package itself. This aspect has been investigated experimentally, since the constraints applied to the ribs by the packaged membrane are not easily simulated. It appears that this should not be a serious problem. Secondly, there is the possibility that the membrane might go past the hub during deployment and, having deployed too far outwards, be unable to flip back to the front of the hub, remaining in a concave —rather than convex— shape. This problem is potentially serious and, indeed, many of our deployment tests have shown this kind of problem, see Section 4.5. It is believed that this problem can be minimised by reducing the hub diameter further than required purely from prestressing considerations. Also, it should be possible to find optimal fold positions in the ribs in order to eliminate this problem. However, packaging efficiency is likely to be reduced. A good understanding of the deployment dynamics and good simulation models will be required, before such optimisation can be carried out.

Scheme 3 appears to be, potentially, the best in this respect. It is expected that the offset from the hub associated with the pre-folding of the membrane will force deployment into the required convex shape.

At the end of Phase (i) of the study a meeting was held at ESTEC and it was decided that only Scheme 2 would be investigated during Phase (ii).

3.6 Experimental verification of Scheme 2: folding apparatus

A folding model of the CRTS reflector was made to verify the second packaging scheme. The geometric properties of the model are as given in Section 1. The model differs in two respects from the actual reflector. First, it has straight, instead of parabolically curved ribs, and hence the six gores become flat when the model is fully deployed. This is because the manufacture of doubly-curved ribs is considerably more complex than the manufacture of singly-curved ribs. The small longitudinal curvature of the actual ribs is not expected to have a significant effect on deployment properties, but this assumption ought to be further investigated at a later stage. Second, the model does not have an automatic hub contraction/expansion mechanism, and hence the membrane cannot be prestressed automatically when deployment is terminated. This is not at all a problem for the present study and, furthermore, it is possible to adjust the position of each rib to investigate the effects of changing the hub radius on the dynamics of deployment. Each rib is separately mounted onto an Al-alloy cylindrical element with a flat machined on the bottom side. This element is connected by two bolts to an Al-alloy disk with six radial slots.

A simple folding apparatus has also been made, Fig. 18, to fold the model according to the pattern of Scheme 2. The apparatus consists of two Al-alloy tubes, on either side of the hub disk. A set of wires, connected to the ribs at the positions where the various folds have to be formed, pull the ribs up or down. Figure 18 shows the model with the folding apparatus. All required fold lines are formed while the ribs are held in position by the wires. Each rib is pulled down by two wires and up by one wire. The folding pattern that is being tested is similar to that shown in Figs 7-8, but requires only three folds in each rib, not four . The first fold is near the hub. All concave and convex folds have been marked on the membrane before starting the folding operation.

For this fold pattern, the expected values of the package height and diameter are, Eqs 13-14

$$D = 2R + 2nr = 2 \times 47.5 + 2 \times 3 \times 12 = 167 \text{ mm}$$

$$H = \frac{L}{n} = \frac{540}{3} = 180 \text{ mm}$$

while the actual values, measured after packaging the model, see Fig. 18(c), are

$$D = 185 \text{ mm}$$

$$H = 160 \text{ mm}$$

The small discrepancies between estimated values and actual values are explained as follows. H is

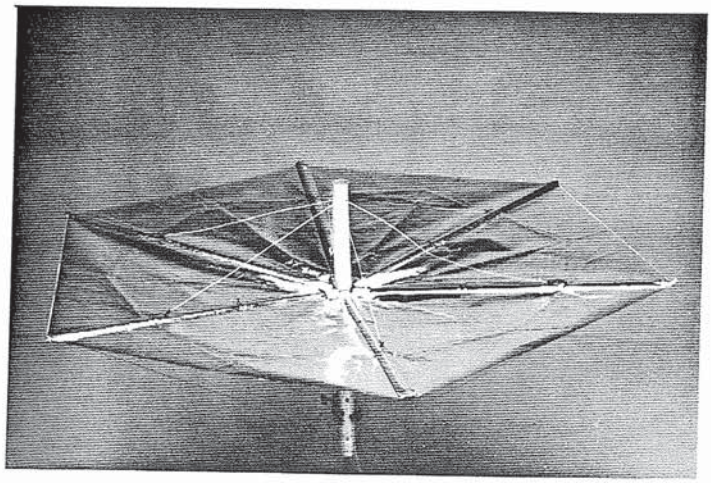

(a)

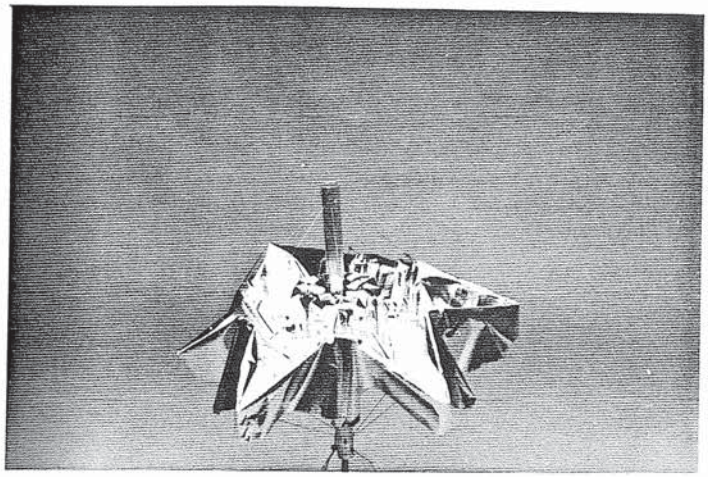

(b)

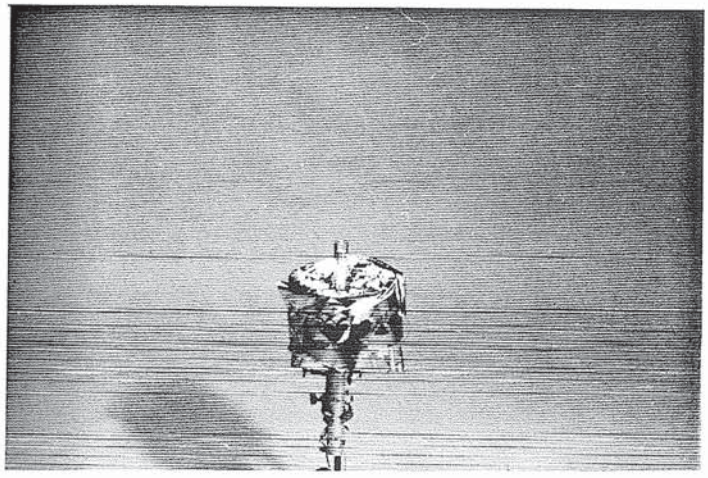

(c)

Fig. 18. Folding apparatus for Scheme 2. The ribs are pulled up and down by wires connected to a central tube.

smaller than expected because Eq. 13 does not allow for the arc length of the folds. D is bigger than expected because Eq. 14 does not include the length of the transition zone, at the connection between a rib and the hub. This transition zone is shown clearly in Fig. 9.

4. DEPLOYMENT STUDIES

Phase (ii) of the study has investigated several aspects related to the deployment dynamics of a CRTS reflector, both by theory and experiment. Experiments are essential for work of this kind, because the large-displacement mechanical behaviour of a thin-walled rib has some unusual features, see Section 4.2, which will have a crucial effect on the deployment dynamics of the CRTS reflector. If incorrectly modelled, these special features can lead to large inaccuracies in the predicted behaviour. A theoretical analysis, based on realistic assumptions is also essential. Apart from the usual, general reasons for pursuing a theoretical approach, such as the need to perform parametric studies in order to select optimal system parameters, in this particular project only a theoretical model can simulate the deployment in a gravity-free environment. It would be practically impossible to set up a test where the effects of gravity on a very flexible structure such as one of the ribs of the CRTS reflector, are cancelled while the rib undergoes a large motion.

Sections 4.1-4.4 address a series of fundamental issues related to the deployment of a rib with a single fold. Sections 4.5-4.6 investigate the deployment of 1 m and 5 m reflectors.

4.1 Deployment experiments on 0.53 m rib

A series of simple "deployment" tests were carried out on a single CuBe rib attached at one end to a cylindrical element. Similar elements are used for the hub of the 1 m model (see Section 3.6). The root element was held fixed, with the rib vertical and pointing upwards, and a 90° fold was formed in the rib, approximately in the middle. The rib was held in this position by a tip support and, when the support was released, a single photograph of the deployment sequence was taken, with a Polaroid camera. The experiment took place in a dark room, and the shutter of the Polaroid was held open throughout the experiment. A strobe light gave one flash every 4/100 s. The rib was initially folded on its *strong* side (see Section 4.2).

Figure 19 shows a photograph obtained by this technique. The first five rib configurations are clearly visible, and have been sketched in Fig. 20. After that, the rib bent to the left (i.e. on its *weak* side, see Section 4.2) and, after slowly returning towards the upright configuration, it underwent a high-frequency, small-displacement oscillation about the vertical. A lateral-torsional vibration of the rib is often noticed towards the end of such tests. It is probably triggered by a small asymmetry in the reverse fold.

The deployment process is divided into three phases. During the first phase the fold travels towards the root. The fold is a localised region of high curvature that divides the rib into two parts, which are approximately straight. During the second phase the rib rotates as a rigid body about a point near the root. During the third phase the rib vibrates as a slender cantilever.

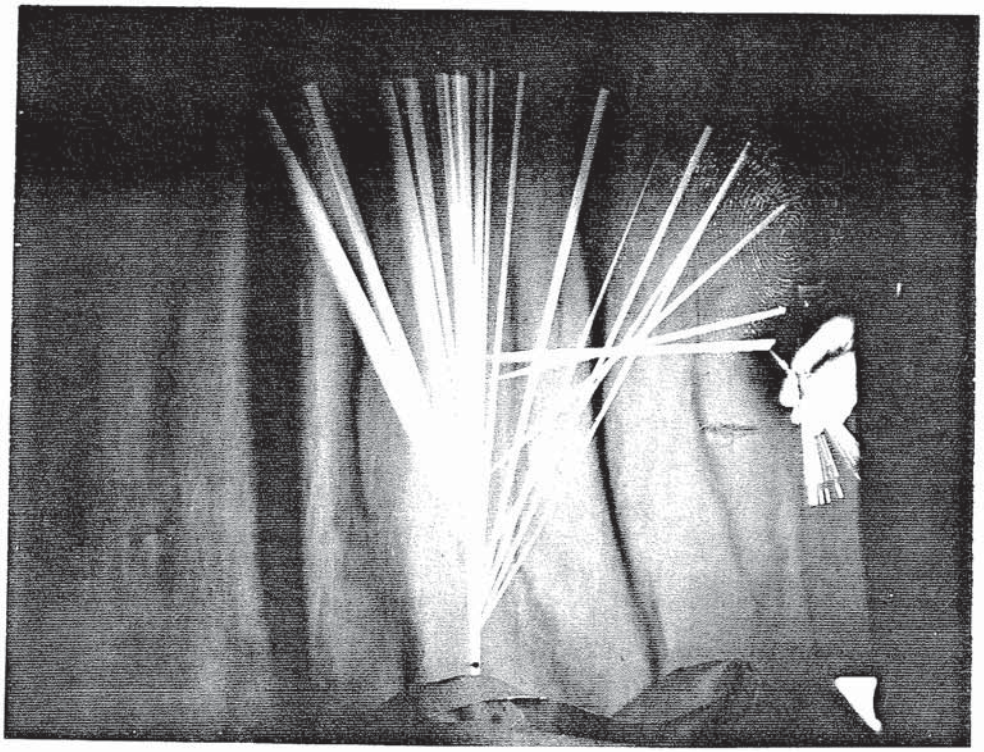

Fig. 19. Multiple exposure photograph of simple "deployment" test on rib with a single fold. The interval between successive shapes is 0.04 s.

Figure 20 shows five configurations of the rib, at intervals of 4/100 s, during the first phase. The first configuration is the initial, "folded" configuration with a 90° fold. In the final configuration, at t = 0.16 s, the travelling fold has just reached the root. It is essential that this behaviour should be predicted accurately by the theoretical model, because the largest accelerations, and hence inertia loading on the rib, occur during this phase. The second phase begins at t = 0.16 s and, although the experimental technique is too coarse to provide much information, it can be worked out from Fig. 19 that the rib becomes approximately straight during the second phase, at $t \cong 0.32$ s.

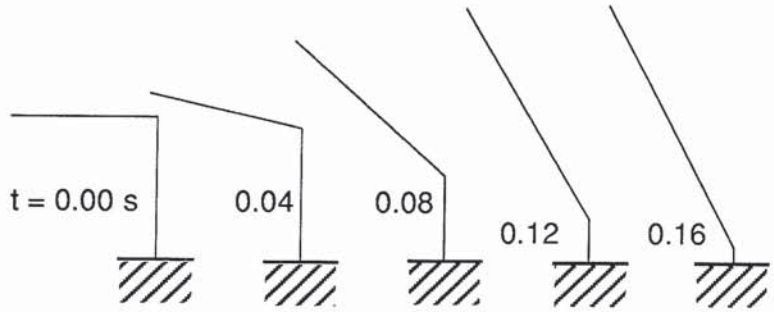

Fig. 20. Sketch of first five rib configurations, during deployment

4.2 Moment/Curvature relationship for a rib

A good understanding of the moment/curvature relationship for a rib is essential before one attempts to study its deployment behaviour. Basically, a rib is a thin-walled, open-section beam, whose cross-section is an arc of a circle. Some properties of such beams are well known. For example, it is known that they show a kind of instability when subject to bending within the plane of symmetry of the cross-section. As the load is increased, there is a tendency for the cross-section to become flatter, and at a critical value of the load the beam snaps [6]. In the post-buckling range the beam is unable to carry much lateral load. Also, the critical load is higher if the beam is bent in the concave direction.

Another known property of these beams is that, after buckling, their deformation tends to localise in a small region whose longitudinal curvature is exactly the same as the transverse curvature 1/r of the rib unstressed. This region has no transverse curvature, and behaves like a constant-moment hinge [7,8]. It is joined on either side to practically straight parts of the rib by transition regions 2r-3r long. If the angle of relative rotation between one end of the rib and the other end is increased, or decreased, the length of the hinge region increases, or decreases, accordingly. This property is exploited in tape measures, constant tension springs (Tensators) and deployable booms [9].

To characterise further the behaviour of the ribs of the model reflector two sets of tests were conducted. The first test measured the relationship between the bending moment M and the relative rotation θ between the ends of a 140 mm long rib with transverse radius of curvature r = 12 mm. The ends of the rib were embedded in Perspex blocks. This element was tested in four point bending, as shown in Fig. 21(a). The end blocks were slowly rotated by applying two downward forces of equal magnitude F, in a displacement-controlled mode. After that each block had rotated

through about 1 rad, the rotation rate was reversed. The values of F and the horizontal component of the distance between each support and the nearest point of application of the load were measured for each rotation increment, and hence the corresponding (uniform) bending moment in the rib was calculated. This rib element was tested twice, first with the concave side facing down, and then up. The results of this experiment are shown in Fig. 22(a).

For a rib bent on the convex side ($\theta > 0$) M increases up to 700 Nmm and $\theta = 0.2$ rad, approximately linearly. Then the rib snaps with a loud "click" and M drops to about 25 Nmm while the deformation localises in a short, longitudinally curved region. Then, M slowly increases to 32 Nmm, and then remains constant at this value. Note that in Fig. 22(a) the value of θ increases suddenly when the rib snaps, due to the elasticity of the testing system. When the rotation rate is reversed, M remains constant until $\theta = 0.2$ rad, at which point the rib snaps back into a transversally curved configuration, i.e. the region of localised deformation suddenly disappears. Due to the elasticity of the testing machine, though, M does not return to the peak value reached on loading.

For a rib bent on the concave side, i.e. $M < 0$ and $\theta < 0$, there is a sudden snap at a limit moment of about −200 Nmm, then the rib gradually softens and finally M becomes approximately constant at 14-15 Nmm, for $|\theta| > 0.5$ rad. The unloading path is practically identical to the loading path.

The behaviour of the rib is entirely elastic, as would be expected for 0.1 mm thick, Cu-Be ribs with r = 12 mm [9].

A similar set of tests on a 210 mm rib, also embedded in rigid end blocks, showed no significant difference. Hence, it was concluded that end effects were negligibly small in the test of the 140 mm rib. It is expected that the behaviour of a much shorter rib, where the transition regions on either side of the hinge region cannot form fully, would be quite different because of the constraint imposed by the end blocks.

The above measured values of the bending moments associated with a steady-state growth of the fold regions will be denoted by

$$M^+ \cong 30 \text{ Nmm}$$

and

$$M^- \cong 15 \text{ Nmm}$$

These values are a little lower than the following estimates, based on formulae adapted from Rimrott [9]

$$M^+ = \frac{E}{1-\nu}\frac{\pi t^3}{18} = \frac{131\cdot 10^3 \cdot \pi \cdot 0.1^3}{(1-0.3)\cdot 18} = 32.7 \text{ Nmm} \qquad (25)$$

$$M^- = \frac{E}{1+\nu}\frac{\pi t^3}{18} = \frac{131\cdot 10^3 \cdot \pi \cdot 0.1^3}{(1+0.3)\cdot 18} = 17.6 \text{ Nmm} \qquad (26)$$

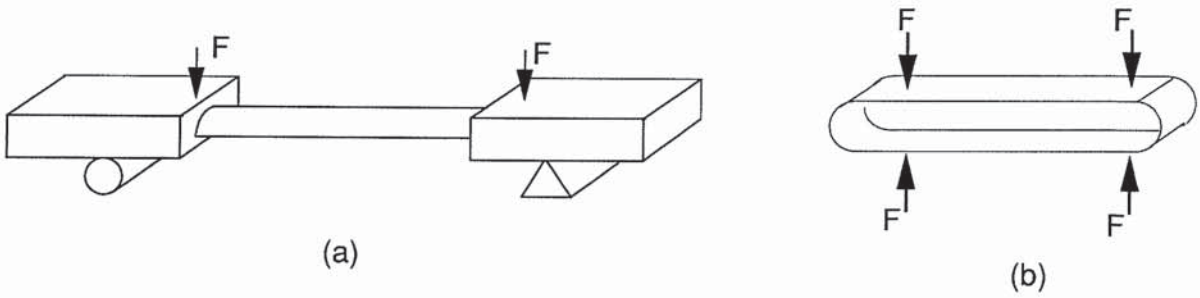

Fig. 21. Schematic diagram of tests to measure the moment/curvature relationship for a rib. (a) Four-point bending test with rib embedded into rigid blocks. (b) Test of rib loop, to increase the curvature of the hinge region.

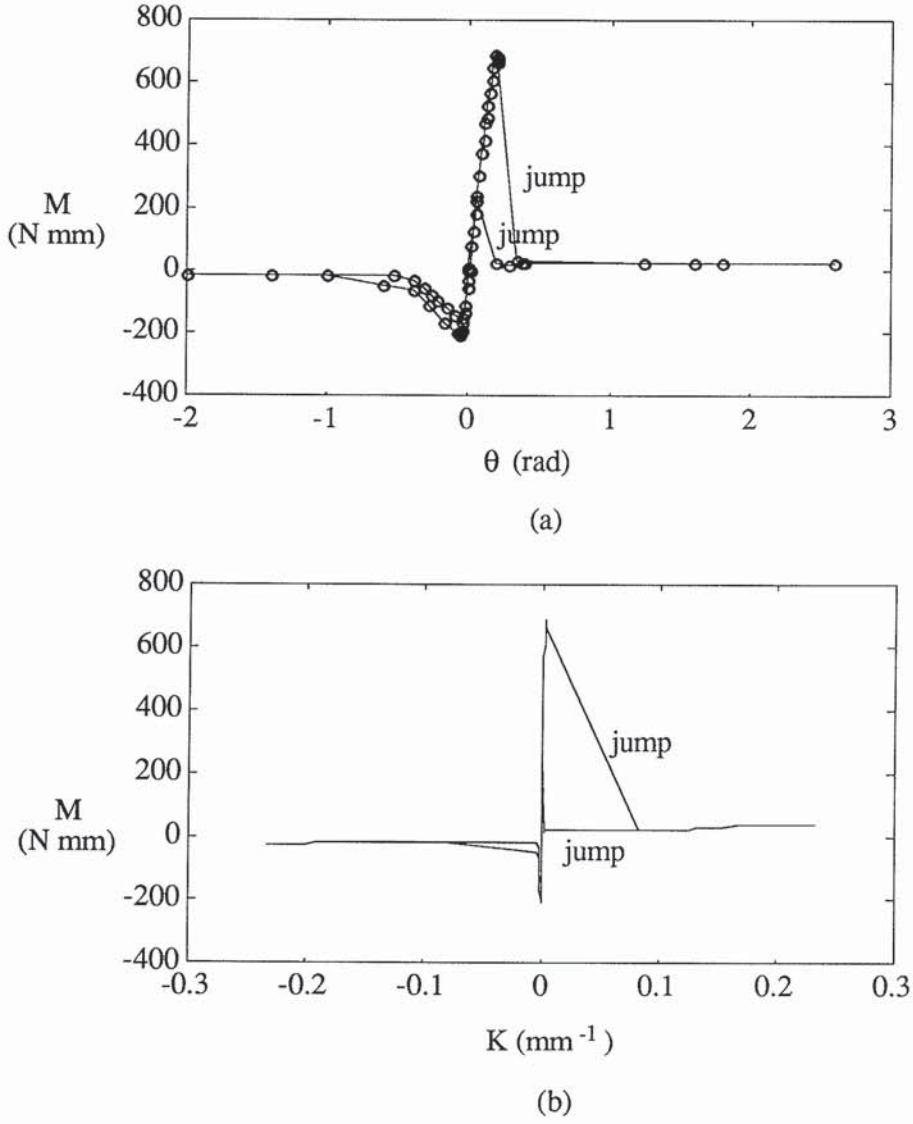

Fig. 22. (a) Moment/rotation and (b) moment/curvature relationship for a rib.

Even though M^+ and M^- correspond to several different points in the M/θ plot, actually all of these points would map into a single point of a moment/curvature plot, because the curvature in the hinge region remains constant while θ increases.

To characterise the full moment/curvature (K) relationship for the rib, it is necessary to distinguish between the behaviour of the rib before and after the deformation has localised. Up to the point where the deformation localises in a small region, the linear part of $M(\theta)$ can be re-plotted by dividing all values of θ by the rib length, thus obtaining the average curvature of the specimen. See Fig. 22(b). The remaining part of $M(\theta)$ produces only two more points when re-plotted in terms of K, as explained above.

To obtain further points it is necessary to increase the curvature in the hinge region, which was done in a separate test. A schematic diagram of the set up is shown in Fig. 21(b). Two folds were formed in a 250 mm long rib and then the ends of the rib were joined together, to form a continuous loop. The loop was loaded by two forces of equal magnitude F, at the top, and supported by knife edge and roller supports, at the bottom. During the test, also in displacement-controlled mode, the loop was compressed by varying the value of F. At each step, the curvature at the centre of the hinge regions was measured by means of a curvature gauge, together with the force F and the distance between hinge centres. From these measurements the maximum value of the bending moment in the folds can be calculated. At the start of the test the loop is subject to a uniform bending moment M^+ (or M^-), and during the test M increases only in the hinge regions. The moment is maximum at the centre of each fold. The largest measured value of M was 44 Nmm, with the rib nearly at the yield point.

The additional points obtained by this test are also plotted in Fig. 22(b). After the deformation of the rib has localised, i.e. for $|K| > 1/12\ \text{mm}^{-1}$, M gently increases with $|K|$.

4.3 Simulations with ABAQUS

Finite element simulations of the test described in Section 4.1 were carried out using the package ABAQUS (version 5.2).

The rib was modelled by a mesh of 23 (or 43) elastic beam elements of equal length, whose non-linear moment-curvature relationship was specified according to Fig. 22(b). The rib was initially straight and unstressed. Initially, both elements B21 and B23 were used, i.e. two-dimensional beam elements based respectively on linear and cubic shape functions. The two elements gave very similar results, and the lower-order element perfomed better for some analyses. Hence, element B21 was selected and all results presented in this report were obtained with this element.

To form a 90° fold, two rotational constraints were applied to the nodes of the element in the middle of the rib. Then, the constraint nearer to the tip of the rib was rotated through 90° in a series of steps, while the other constraint was held fixed. Then, both constraints were released simultaneously, thus starting the free deployment of the rib. Both gravity and air drag effects were

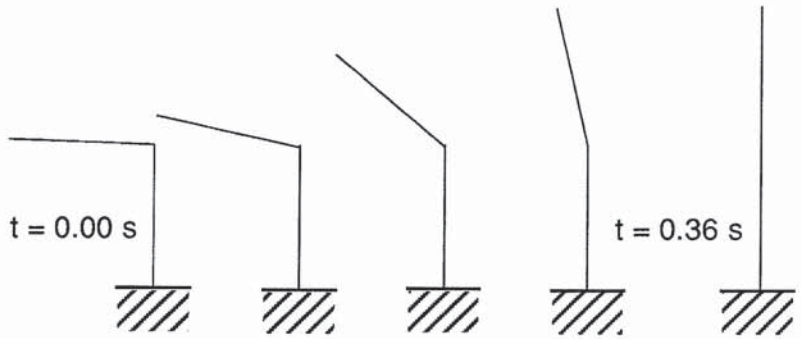

Fig. 23. Deployment sequence predicted by f.e. analysis.

included in the simulation, even though only the effects of gravity are really significant.

The results, shown in Fig. 23, were rather disappointing. The fold did not move at all, and hence the predicted deployment was a pure rigid-body rotation of the half rib that had been rotated. The total predicted deployment time was 0.36 s, which is quite accurate.

A careful analysis of these results shows that the ABAQUS prediction is consistent with the model that has been analysed, but the explanation is quite subtle. In the model the fold does not move because the actual propagation mechanism, based on the softening of the rib near an existing fold, is not allowed for. In the model a new fold can form only if the bending moment reaches the limit value. Hence, for an existing fold to move along the rib according to this model, that fold has to close and a new fold has to form. But this requires a large bending moment, which is practically impossible since the bending moment at the existing fold is quite low.

No explanation has yet been found for the good accuracy of the deployment time predicted by this model, which is quite unexpected since the model does not predict the motion of the fold correctly. Hence, it is not yet known if estimates of deployment times obtained from ABAQUS are generally reliable.

It is expected that a proper, three-dimensional finite element model of the rib, based on shell elements, ought to give more accurate estimates of the deployment process, but it is unlikely that this approach could be adopted for problems of a realistic size. The key difficulty is that, because the fold region is expected to move towards the root, most of the rib has to be modelled by small shell elements, whose size is related to the transverse dimension of the cross section of the rib. To model properly the ovalization of the cross-section, it is necessary to use no fewer than three elements for half of the rib. For a 500 mm long rib about 500 elements would be required. So far, preliminary analyses of meshes of shell elements with fairly elongated shape, to reduce the total number of elements required, have been unsuccessful. These analyses did not achieve convergence, not even for the initial phase of the analysis that simulates the formation of the initial fold.

It is quite possible that these difficulties could be overcome by the design of an optimal mesh for this problem and, possibly, by making use of an automatic mesh updating scheme. But, given the

apparent simplicity of the physical problem that is being modelled, the computer effort required by this approach seems absolutely out of proportion. The next section presents a radically different approach to the problem, based on a two-degree-of-freedom model which can produce results very quickly.

4.4 Analytical model

Figure 24 shows a simple, two-degree-of-freedom model of a rib with a single fold. The fold is idealised as constant-moment, point hinge B located at a variable distance λ from the tip A. The parameter λ is the first degree of freedom of this model. Any deformation of the rib away from the hinge is neglected, and hence AB and BO are treated as rigid bodies. The second degree of freedom is the rotation θ at the hinge.

For simplicity, it will be assumed that the moment at the hinge remains constant, i. e. that $M(\theta) = M^+$ (or M^-), thus neglecting the large moments associated with small values of θ. This assumption could be removed quite easily, if necessary.

The mass of AB (and also of BO) is a variable because the hinge position moves at velocity $\dot{\lambda}$ along OA. Thus, body AB "swallows" a stream of stationary matter and suddenly imparts to it both translational and rotational velocity components. The time rate of mass increase of AB is $\rho\dot{\lambda}$. Therefore, the standard equations of motion for rigid bodies with constant mass cannot be applied directly to AB and BO. Next, we shall derive the dynamic equations appropriate for this system.

We introduce, Fig. 25, the unit vectors **i, j** in the direction of the fixed coordinate system O, x, y, and a unit vector **k** perpendicular to **i** and **j**, and such that **i, j, k** form a right hand set. We also introduce the auxiliary unit vectors **e** and **e*** on a moving reference frame with origin B. The orientation of **e, e*** is defined with respect to **i, j** by the angle θ.

The position, velocity and acceleration of a general point P on AB, see Fig. 25, at a distance d = constant from O are as follows

$$\mathbf{r} = (L-\lambda)\mathbf{i} + (d-L+\lambda)\mathbf{e} \tag{27}$$

$$\dot{\mathbf{r}} = -\dot{\lambda}\mathbf{i} + \dot{\lambda}\mathbf{e} + (d-L+\lambda)\,\dot{\theta}\,\mathbf{e}^* \tag{28}$$

$$\ddot{\mathbf{r}} = -\ddot{\lambda}\mathbf{i} + \left[\ddot{\lambda} - (d-L+\lambda)\,\dot{\theta}^2\right]\mathbf{e} + \left[2\dot{\lambda}\dot{\theta} + (d-L+\lambda)\,\ddot{\theta}\right]\mathbf{e}^* \tag{29}$$

These expressions will be used at several stages of the derivation of the equations of motion.

The equations of motion of variable mass systems are usually derived [10] either by considering the force and moment interaction between a part of the system whose mass remains constant, i.e. body AB at time t, and the incoming mass over a short time Δt, or by differentiation of the linear and angular momentum of a control volume that encloses a constant mass, i.e. body AB at time t plus the mass $\rho\dot{\lambda}\Delta t$ that joins AB during the time Δt. Both approaches are suitable for the present

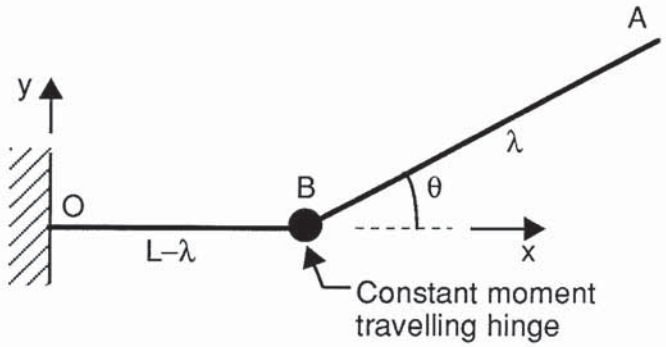

Fig. 24. Two d.o.f. model of deployment of a rib with a single hinge. The model parameters are λ, θ.

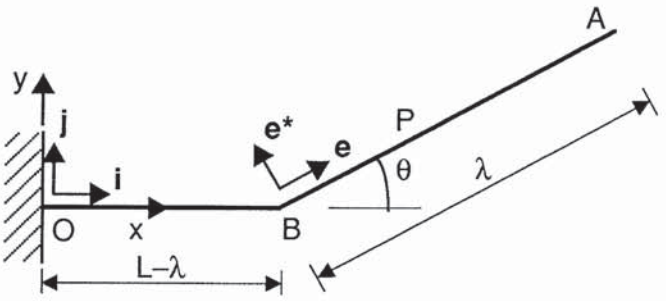

Fig. 25. Definition of fixed and moving reference frames for two d.o.f. model.

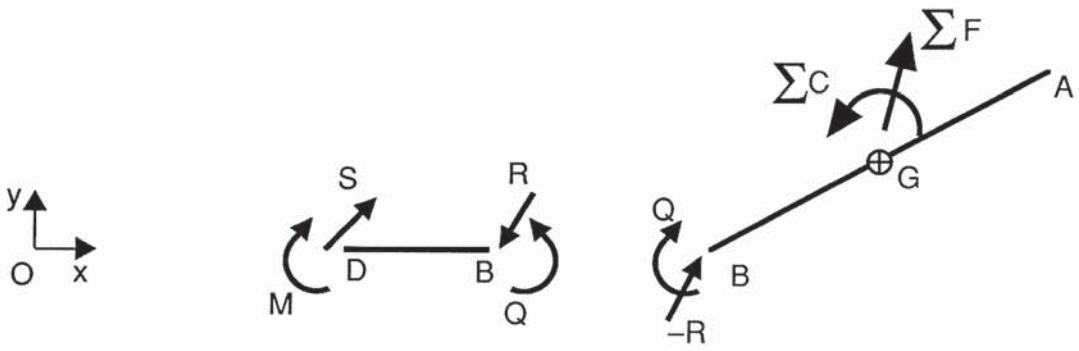

Fig. 26. Free body diagrams for two d.o.f. model, at time t. During Δt the hinge moves from B to D.

situation, but the first approach provides greater physical insight and hence will be followed here.

Figure 26 shows two free body diagrams for the system at time t. The hinge is at B, at time t, and moves to D at time $t+\Delta t$. Body AB has length λ and mass $\rho\lambda$. It is subject to an external force resultant $\sum\mathbf{F}$ and to an external couple $\sum\mathbf{C}$ about its centre of mass, and also to force and moment interactions $-\mathbf{R}$ and Q with body BD. The external forces and couples result from, e.g., gravity and air drag. Body BD, of length $\dot{\lambda}\Delta t$ and mass $\rho\dot{\lambda}\Delta t$, is subject to forces and moments **S**, M at D and **R**, Q at B, which are applied to BD by bodies OD and AB, respectively. The effects of external distributed forces on this short body are negligible in the present analysis.

The stress resultants behind the hinge, i.e. at point B, and ahead of the hinge, at point D, can be calculated from **R**, **S**, M and Q. Although the above formulation allows for discontinuities in both

axial/shear forces and bending moment, it will be shown that the bending moment is in fact continuous across the hinge.

Body BD is stationary at time t. During the time increment Δt body BD is subject to an impulse $(\mathbf{R}+\mathbf{S})\Delta t$ which accelerates it to a velocity $\cong \dot{\mathbf{r}}_B$, where $\dot{\mathbf{r}}_B$ is the velocity of point B. Hence, equating impulse to change of linear momentum, we obtain

$$\mathbf{R} = \rho\dot{\lambda}\dot{\mathbf{r}}_B - \mathbf{S} \tag{30}$$

Also, the impulsive couple about O is approximately

$$\left[r_B \times (\mathbf{R}+\mathbf{S}) + (Q-M)\,\mathbf{k}\right]\Delta t \tag{31}$$

and the change in moment of momentum about O is

$$\mathbf{r}_B \times \rho\dot{\lambda}\Delta t\,\dot{\mathbf{r}}_B \tag{32}$$

Equating Eqs 31 and 32, and substituting

$$\mathbf{r}_B = (L-\lambda)\mathbf{i} \tag{33}$$

and

$$\dot{\mathbf{r}}_B = -\dot{\lambda}\mathbf{i} + \dot{\lambda}\mathbf{e} \tag{34}$$

we obtain

$$M = Q \tag{35}$$

Next, we turn to body AB and, since it has constant mass, we write its equations of motion in the standard form

$$\sum \mathbf{F} - \mathbf{R} = \rho\lambda\ddot{\mathbf{r}}_G \tag{36}$$

$$\left(\sum C - Q\right)\mathbf{k} + \left(\mathbf{r}_B - \mathbf{r}_G\right)\times(-\mathbf{R}) = I_G\ddot{\theta}\,\mathbf{k} \tag{37}$$

where I_G is the moment of inertia of AB about G.

Substituting Eq. 30 into Eq. 36

$$\sum \mathbf{F} + \mathbf{S} = \rho\dot{\lambda}\dot{\mathbf{r}}_B + \rho\lambda\ddot{\mathbf{r}}_G \tag{38}$$

and, substituing Eq. 34 and

$$\ddot{\mathbf{r}}_G = -\ddot{\lambda}\mathbf{i} + \left(\ddot{\lambda} - \frac{\lambda}{2}\dot{\theta}^2\right)\mathbf{e} + \left(2\dot{\lambda}\dot{\theta} + \frac{\lambda}{2}\ddot{\theta}\right)\mathbf{e}^* \tag{39}$$

into Eq. 38, we obtain

$$\frac{\sum \mathbf{F} + \mathbf{S}}{\rho} = -\left(\dot{\lambda}^2 + \lambda\ddot{\lambda}\right)\mathbf{i} + \left(\dot{\lambda}^2 + \lambda\ddot{\lambda} - \frac{\lambda^2\dot{\theta}^2}{2}\right)\mathbf{e} + \left(2\lambda\dot{\lambda}\dot{\theta} + \frac{\lambda^2\ddot{\theta}}{2}\right)\mathbf{e}^* \tag{40}$$

Finally, substituting Eq. 30 and Eq. 35 into Eq. 37, we obtain

$$\left(\sum \mathrm{C} - \mathrm{M}\right)\mathbf{k} + \left(\mathbf{r}_\mathrm{A} - \mathbf{r}_\mathrm{G}\right) \times \left(\rho\lambda\ddot{\mathbf{r}}_\mathrm{G} - \sum \mathbf{F}\right) = \mathrm{I}_\mathrm{G}\ddot{\theta}\,\mathbf{k} \tag{41}$$

and, substituting

$$\mathbf{r}_\mathrm{B} - \mathbf{r}_\mathrm{G} = -\frac{\lambda}{2}\mathbf{e} \tag{42}$$

and Eq. 39 into Eq. 41 we obtain

$$\left(\sum \mathrm{C} - \mathrm{M}\right)\mathbf{k} + \frac{\lambda}{2}\left(\mathbf{e} \times \sum \mathbf{F}\right) = \rho\lambda^2\left(\frac{\ddot{\lambda}\sin\theta}{2} + \dot{\lambda}\dot{\theta} + \frac{\lambda}{3}\ddot{\theta}\right)\mathbf{k} \tag{43}$$

Equations 40 and 43 are the dynamic equations for the two-degree-of-freedom model. Equation 40 is a vector equation, equivalent to two algebraic equations, while Eq. 43 —where all terms are in the **k**-direction— is equivalent to only one algebraic equation. These three equations contain five unknowns: **S**, M, θ, λ. The two unknown components of **S** are equal to the axial force ($-\mathrm{S}_\mathrm{x}$) at a section just ahead of the travelling hinge and to the shear force ($-\mathrm{S}_\mathrm{y}$) also at the same section. Two more equations are required to determine a unique solution. The first condition is that the bending moment at the hinge should have a constant value, i.e.

$$\mathrm{M} = \mathrm{M}^+ \quad \left(\text{or } \mathrm{M}^-\right) \tag{44}$$

The second condition is that the bending moment should be a maximum in the middle of the fold region. Otherwise the hinge would form at a different section, and the shear force would be zero at that section. Hence, the condition is that the component of **S** in the direction of the normal to the rib should be zero in the middle of the fold, or

$$-\mathrm{S}_\mathrm{x}\sin\frac{\theta}{2} + \mathrm{S}_\mathrm{y}\cos\frac{\theta}{2} = 0 \tag{45}$$

Thus, the total number of equations has increased to five, and the problem can be solved.

In practice, there is no need to calculate **S**. A differential equation containing only λ, θ, and their derivatives is obtained by resolving Eq. 40 in the direction at $90° + \theta/2$ to the **i**-direction. This equation has been integrated numerically, together with Eq. 43, using the Runge-Kutta algorithm available in Matlab [11].

To simulate the deployment experiment of Section 4.1 the initial conditions at $t = 0$ were set as follows

$$\frac{\lambda}{\mathrm{L}} = 0.5, \quad \theta = 90°, \quad \dot{\lambda} = \dot{\theta} = 0$$

The results are shown in Fig. 27 for M = 25 Nmm. This time the first two phases of the deployment

sequence were modelled correctly.

According to this prediction, the hinge travels towards the root at increasing speed, until it reaches the root $(\lambda/L = 1)$ at $t \cong 0.12$ s. The hinge rotation at the same time is predicted to be $\theta \cong 27°$. Then, the rib rotates about the root, i.e. λ remains constant, until θ becomes zero at $t \cong 0.20$ s. The third phase of the deployment process, during which the rib oscillates about the final, equilibrium position, has not been modelled in the present analysis. The measured and predicted response are compared in Table 2.

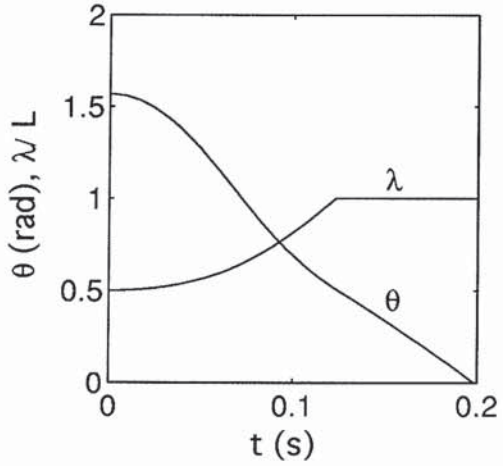

Fig. 27. Rib deployment predicted by two d.o.f. model.

Given the fairly crude assumptions of this analytical model, these results are quite promising and would justify a refinement of the above analysis. A more accurate experimental technique will be needed in future.

To conclude it is noted that, although the equations of motion presented in this section were developed for a rib with a single kink, the approach can be extended to ribs with more than one kink.

Table 2. Properties of 0.53 model reflector

		Experiment		Analytical model	
		Start	Finish	Start	Finish
Phase I	t (s)	0	0.16	0	0.12
	λ/L	0.5	1.0	0.5	1.0
	θ	90°	29°	90°	27°
Phase II	t (s)	0.16	0.32	0.12	0.20
	λ/L	1.0	1.0	1.0	1.0
	θ	29°	0	27°	0

4.5 Experiments and simulations for 1 m reflector

A series of deployment tests were carried out on the 1 m model reflector packaged according to Scheme 2 and using the folding apparatus described in Section 3.6. The package was tied with a string and suspended from a horizontal bar. Deployment was initiated by cutting the string. The deployment sequence was recorded with a video camera, at 1/25 s per frame. Selected shots, as well as five 16-frame deployment sequences are included in the Appendix. Each sequence runs from the top left corner to the bottom right. Not all recorded frames have been printed, and hence the time interval between consecutive frames in a sequence is 3/25 s. The reflector was deployed pointing downwards, otherwise gravity effects would have been too large for the root hinges to close.

The five deployment sequences included with this report are fairly typical of the general deployment behaviour of this model. In the first three frames of each sequence the membrane, wrapped around the package, unwraps. Then, the ribs start to deploy. There is a tendency for one or two ribs to move up, past the hub, despite the downward load applied by gravity. Due to the hoop constraint applied by the curved membrane, in sequences 1-4 these ribs are unable to snap back and hence the reflector deploys into an off-nominal shape. Between frames 15 and 16 of these four sequences, the shape of the model has been corrected by applying a small tip force to the rib(s) that had deployed incorrectly. This problem has been discussed already in Section 3.5. In sequence 5 the model deploys (almost) into the correct shape; the only problem is that the rib in the foreground remains folded downwards.

In all five cases membrane unwrapping is complete by frame 3 and hence takes 6/25 s. Deployment is always essentially complete by frame 12 and, excluding the time for unwrapping, rib/membrane deployment takes about 27/25 s.

An analytical model for a rib with three folds is yet to be developed. Hence, an ABAQUS simulation was carried out, along similar lines to Section 4.3. The rib was modelled by 30 linear beam elements. The mass of the membrane was allowed for, by introducing a series of point masses at appropriate nodes. Gravity effects were also included, but air drag could not be included without modelling the membrane as well. Gravity acted vertically down. Figures 28 and 29 are the deployment sequences predicted by this analysis.

First, the moment/curvature relationship of Fig. 22(b) was assumed. For this case, Fig. 28, the simulation predicts that the two intermediate folds disappear from the rib after about 0.33 s from the start of deployment. Then, the rib oscillates between the configurations labelled $t = 0.291$ and $t = 0.330$. In this simulation the rib does not become completely straight because the moment/curvature relationship requires that on unloading M should climb from M^+ to about 200 Nmm before the fold is allowed to disappear.

A second set of results have been obtained, Fig. 29, for a modified moment/curvature relationship where only the loading path is based on Fig. 22(b). On unloading it is assumed that the bending moment remains constant at M^+ (or M^-) until the unloading path joins the linear-elastic part of the

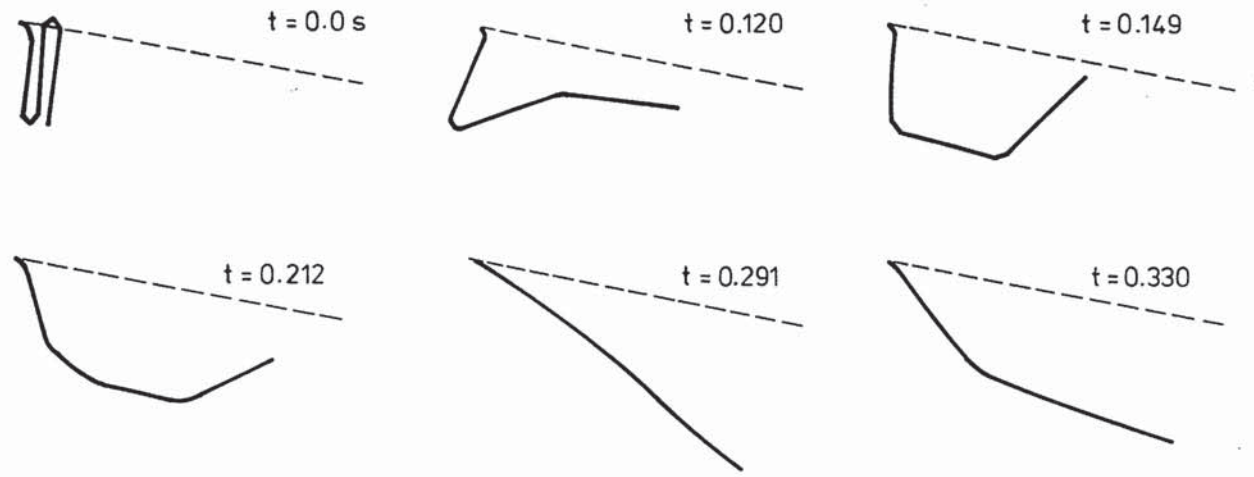

Fig. 28. Finite element simulation of 530 mm long rib with three folds, assuming the moment/curvature relationship of Fig. 22(b).

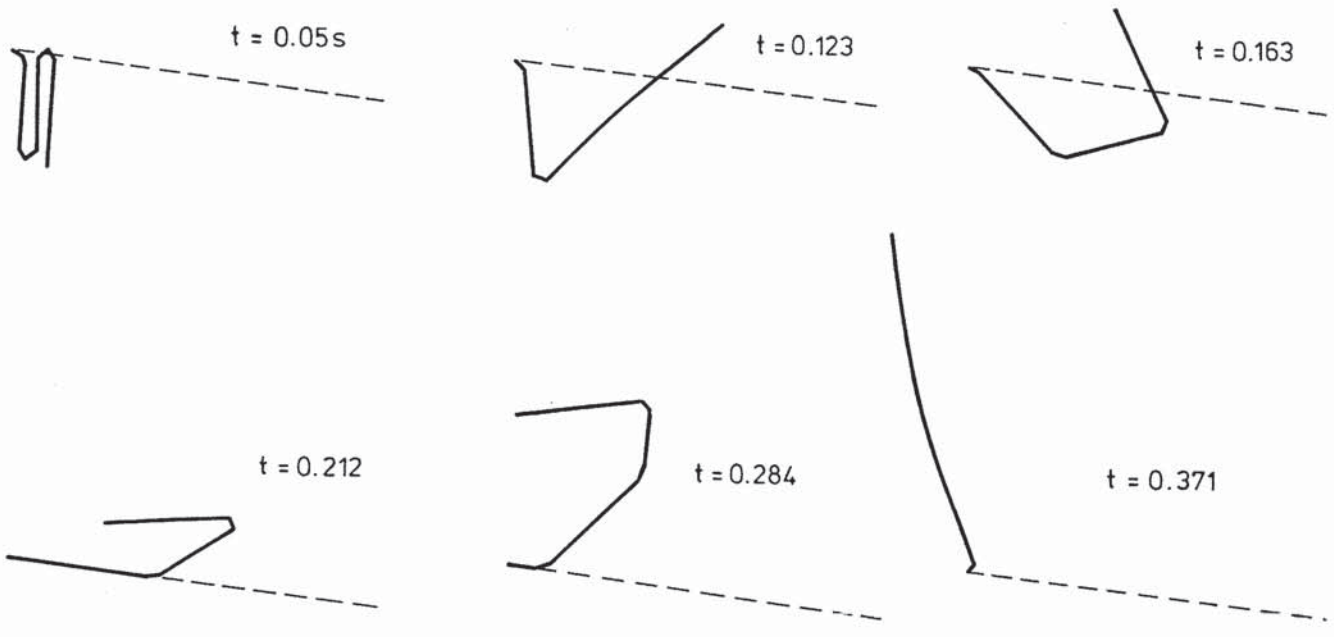

Fig. 29. Finite element simulation of 530 mm long rib with three folds, assuming a modified moment/curvature relationship with constant moment on unloading.

loading curve. In this analysis the rib tends to move upwards, driven by the elastic energy in the hinge near the hub. Although it is expected that the rib will eventually become straight, there was yet no sign of this when the simulation was stopped at t = 0.37 s, with the rib pointing vertically up.

The behaviour predicted in the first part of the second simulation is broadly in agreement with the experimental obsevations on the 1 m model. It can be seen clearly that in all five deployment sequences the tips of several ribs are higher than the hub when the model is approximately half deployed.

A more detailed comparison of experiments and simulation has to be limited to the overall deployment times, which are of the order of 1.0 s in practice and around 0.4 s in the simulations.

4.6 Deployment predictions for 5.5 m reflector

This section presents the results of a preliminary analysis of the deployment of a 5.5 m CRTS reflector, in space. The aim of this analysis is to provide order of magnitude estimates of the deployment properties for a reflector of realistic size.

The design parameters for such a reflector were not yet available when the analysis was carried out, and hence it was decided to use the same properties of the 1 m model reflector, as given in Table 1. Thus, the 5.5 m reflector has six ribs, whose moment/curvature relationship is given in Fig. 22(b). Each rib is 0.1 mm thick and 2.5 m long. Its cross-section has transverse radius of curvature r = 12 mm and subtends an angle of 120°. The hub radius is R = 0.25 m.

In this reflector the mass of the membrane plus ribs is remarkably low: about 1.4 kg for the whole membrane and 0.050 kg for each rib, giving a total mass of about 1.7 kg *excluding the hub*.

If this reflector is packaged according to Scheme 2 with, say, n = 6 folds in each rib, then the size of the packaged reflector, estimated from Eqs 13-14, is

$$D \cong 2R + 2nr = 0.5 + 2 \cdot 6 \cdot 0.012 = 0.64 \text{ m}$$

$$H \cong \frac{2.5}{6} = 0.42 \text{ m}$$

The estimate for D is crucially dependent on the hub diameter, which depends on the size of the hub expansion/contraction mechanism. A preliminary design of this element will be required before a more realistic estimate of package size can be arrived at.

The deployment of a single rib of this reflector has been analysed using ABAQUS, assuming a gravity-free, vacuum environment. In the initial, packaged configuration the rib has six folds. The ABAQUS model included 60 linear beam elements.

The deployment sequence of the rib alone is shown in Fig. 30. Deployment takes about 2.5 s. Figure 31 shows the predicted deployment sequence if the added mass of the membrane is considered in the analysis. In this case deployment takes about 5 s. Hence, it can be concluded that,

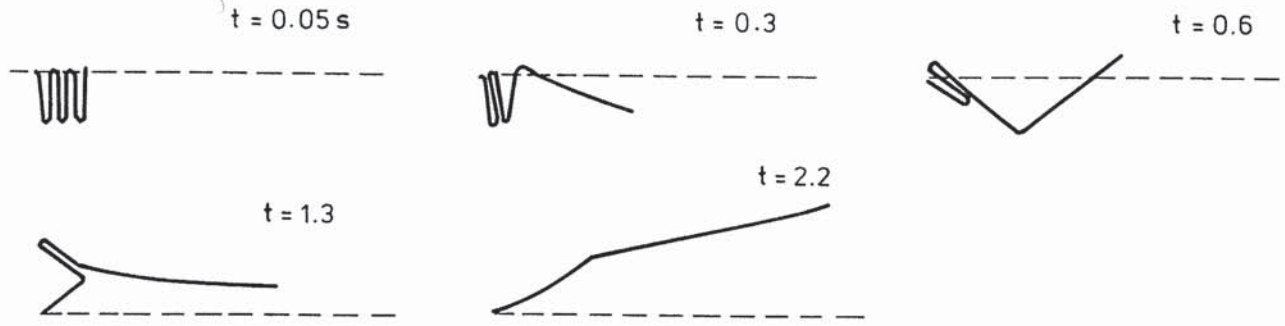

Fig. 30. Finite-element simulation of 2.5 m long rib with six folds, in a gravity-free, vacuum environment.

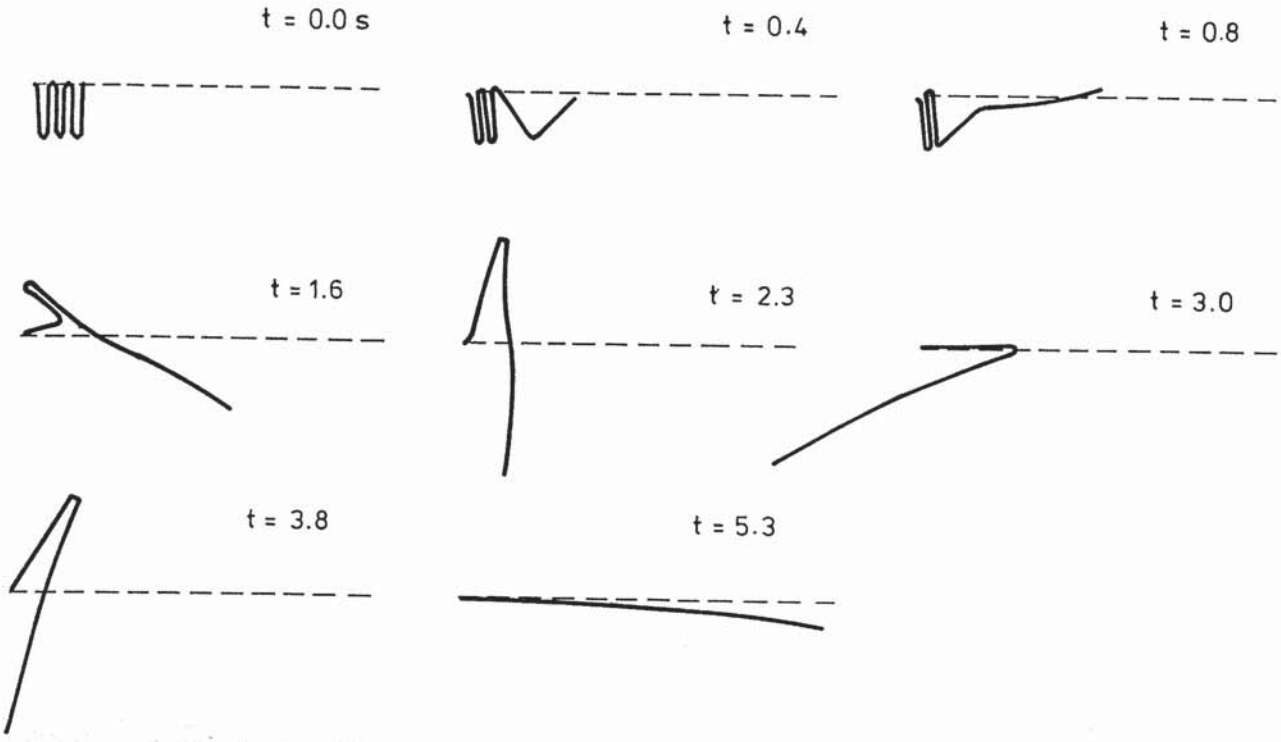

Fig. 31. Finite-element simulation of 2.5 m long rib with six folds, considering the added mass of the membrane.

if the number of ribs is greater than six but the rib properties are unchanged, then deployment will take no less than 2. 5 s and no longer than 5 s. Obviously further work is required to assess the accuracy of these estimates.

In both Figs 30-31 it can be noticed that during the initial stages of deployment the gaps between adjacent parts of the rib tend to close but, because deployment is being simulated as purely two-dimensional, the rib has not been allowed to go over itself by imposing unilateral constraints between different beam elements.

5. CONCLUSIONS AND RECOMMENDATIONS

All of the objectives stated in the Study Definition Document [2] have been achieved. In addition, considerably more experimental work has been conducted than originally envisaged. Two selected folding schemes have been validated experimentally and a folding apparatus has been developed for the most favoured concept. Also, the key patterns of deployment behaviour of the ribs of the reflector have been observed. Based on these properties, an efficient and yet accurate analytical model for deployment analysis has been established.

More detailed conclusions and recommendations for future work are given below.

Three packaging methods for CRTS reflectors have been identified and analysed in detail. Each method is based on a folding pattern whose geometry has been fully worked out and hence can be implemented without difficulty. A trade-off between the three packaging methods has been carried out. The selected packaging scheme (Scheme 2 involving a zig-zag folding of each rib) is the best in terms of ease of implementation and is joint best in terms of packaging efficiency. A simple folding apparatus has been developed to implement this packaging scheme and, with it, the folding operation has been repeated many times on a 1 m model reflector. Deployment tests have been carried out on the model, packaged in this way. During these tests, often the model ended up in off-nominal configurations because some ribs had gone too far past the hub, and were then unable to snap back to the front. It is believed that this anomaly can be resolved by contracting the hub further than required from considerations of prestress alone, and/or by altering the location of the folds in the ribs. This is an area in need of further investigation.

Alternatively, these difficulties could be by-passed by selecting a different, more complex packaging scheme (Scheme 3, involving the wrapping of the membrane and ribs around the hub) whose deployment behaviour is expected to be better synchronised. It is suggested that further consideration be given to this alternative scheme.

As a preliminary, crucial step towards a global understanding of the deployment behaviour of a CRTS reflector, this study has focussed on the deployment of a single rib.

A detailed experimental investigation of the large displacement, large rotation behaviour of a rib has been carried out, leading to a full characterisation of the moment/rotation relationship of the rib. For small rotations, the rib behaves initially in a linear-elastic fashion and then shows a limit point.

For large rotations, the rib forms a localised "*elastic hinge*" where the curvature of the rib —which is in the transverse direction when the rib is unstressed— is now in the longitudinal direction. The bending moment carried by the hinge remains practically constant as the rotation angle is increased. The curvature in this region remains *constant* while the rotation increases. A special test has been devised, to further increase the longitudinal curvature at the hinge and to measure the corresponding bending moments. This test has shown that the bending moment at the hinge is at a minimum when the radius of curvature of the rib in the longitudinal direction is equal to the transverse radius of curvature of the rib unstressed. This property provides an effective mechanism for shielding the rib from high stresses during deployment. At any time t the hinge moves to a position such that the bending moment is equal to this minimum value.

Numerical investigations of the deployment process have been carried out with the ABAQUS finite element package. Also, an analytical technique has been developed specially for this study. Deployment experiments on small scale ribs with a single fold have proved to be most valuable in validating the numerical models. Rather surprisingly, it has been found that the non-linear dynamic finite element analysis is much less accurate than the two-degree-of-freedom analytical model. It is suggested that this analytical model be extended to model ribs with several kinks, and that a more accurate set of experiments be carried out, to further validate this approach.

Once this analytical tool has been fully developed, it will be possible to choose the best location of the hinges in the ribs, to achieve an optimal deployment behaviour.

Finally, concerning the deployment dynamics of a complete reflector, the constraints on rib deployment imposed by the membrane will have to be considered. Also, it will be necessary to include air-drag effects on the membrane in the theoretical simulation of deployment, so that ground tests can be analysed with greater accuracy. An alternative would be to conduct the next series of tests in a vacuum chamber.

REFERENCES

1. ESA (1992). CRTS Patent Application. 9203506 (France) and 08/035,315 (USA).

2. Rits, W.J. (1992). Study of the folding and deployment aspects of a Collapsible Rib Tensioned Surface (CRTS) Antenna reflector: Study Definition Document. YME/WR/2029-issue 2-December 1992.

3. Calladine, C. R. (1983). *Theory of Shell Structures*, Cambridge University Press, Cambridge.

4. Miura, K. (1989). A note on intrinsic geometry of Origami. In *Proc. First International Meeting of Origami Science and Technology*, Ferrara, Italy.

5. Guest, S. D. and Pellegrino, S. (1992). Inextensional wrapping of flat membranes. In *Proc. First International Seminar on Structural Morphology*, Montpellier, La Grand Motte, 7-11 September 1992 (Edited by R. Motro and T. Wester), pp 203-215.

6. Rimrott, F. P. J. (1966). Two Secondary Effects in Bending of Slit Thin-Walled Tubes. *ASME J. Appl. Mech.* March 1966, 75-78.

7. Rimrott, F. P. J. (1970). Querschnittsverformung bei Torsion offener Profile. *ZAMM* **50**, 775-

778.

8. Calladine, C. R. (1988). The theory of thin shell structures 1888-1988. *Proc Instn Mech Engrs* **202**, 1-9.

9. Rimrott, F. P. J. (1966). Storable tubular extendible members. *Engineering Digest* .

10. Meriam, J. L. (1975). *Dynamics*, Second edition (SI version). J. Wiley.

11. Matlab (1989). Matlab User's Guide, The MathWorks.

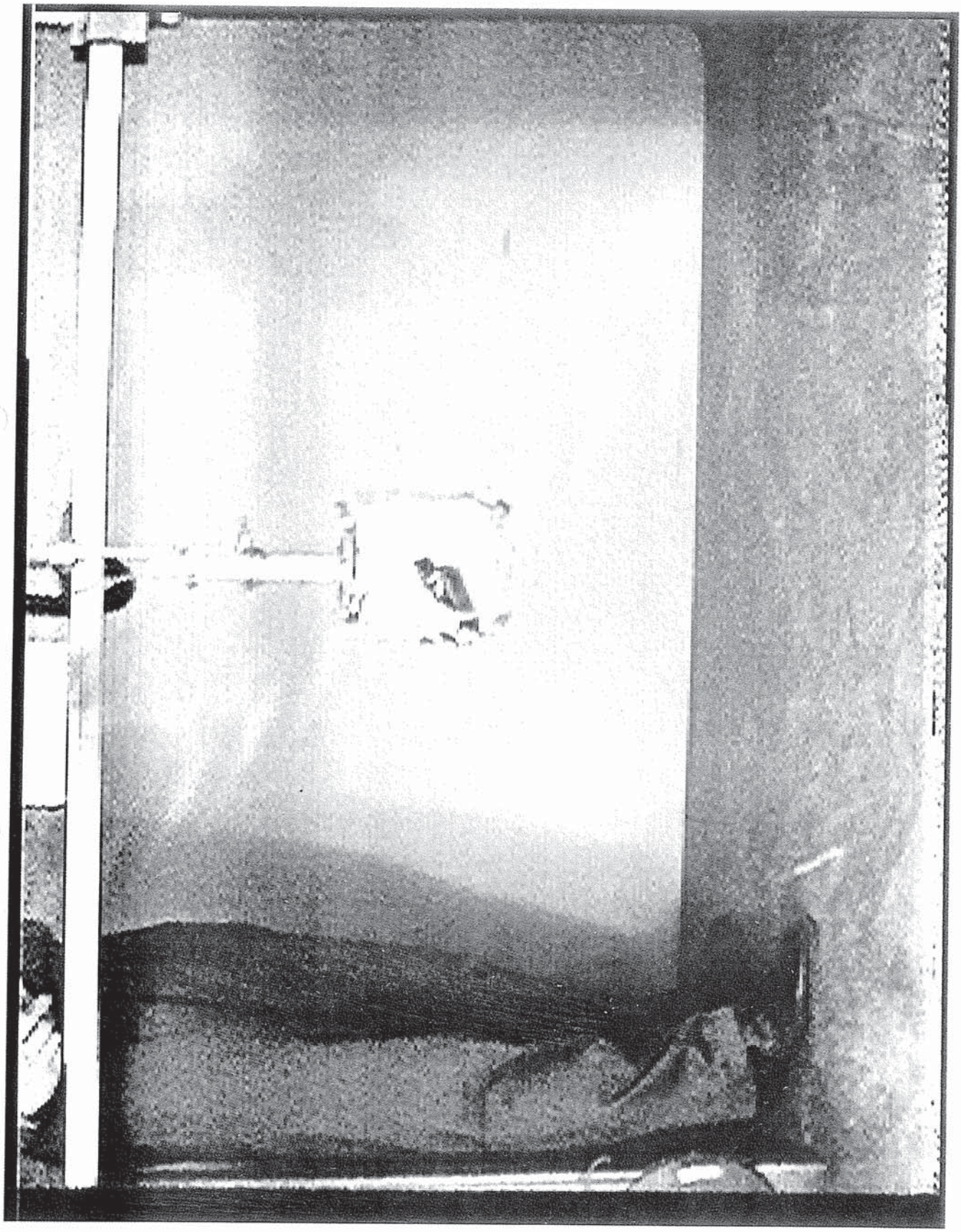

Packaged model.

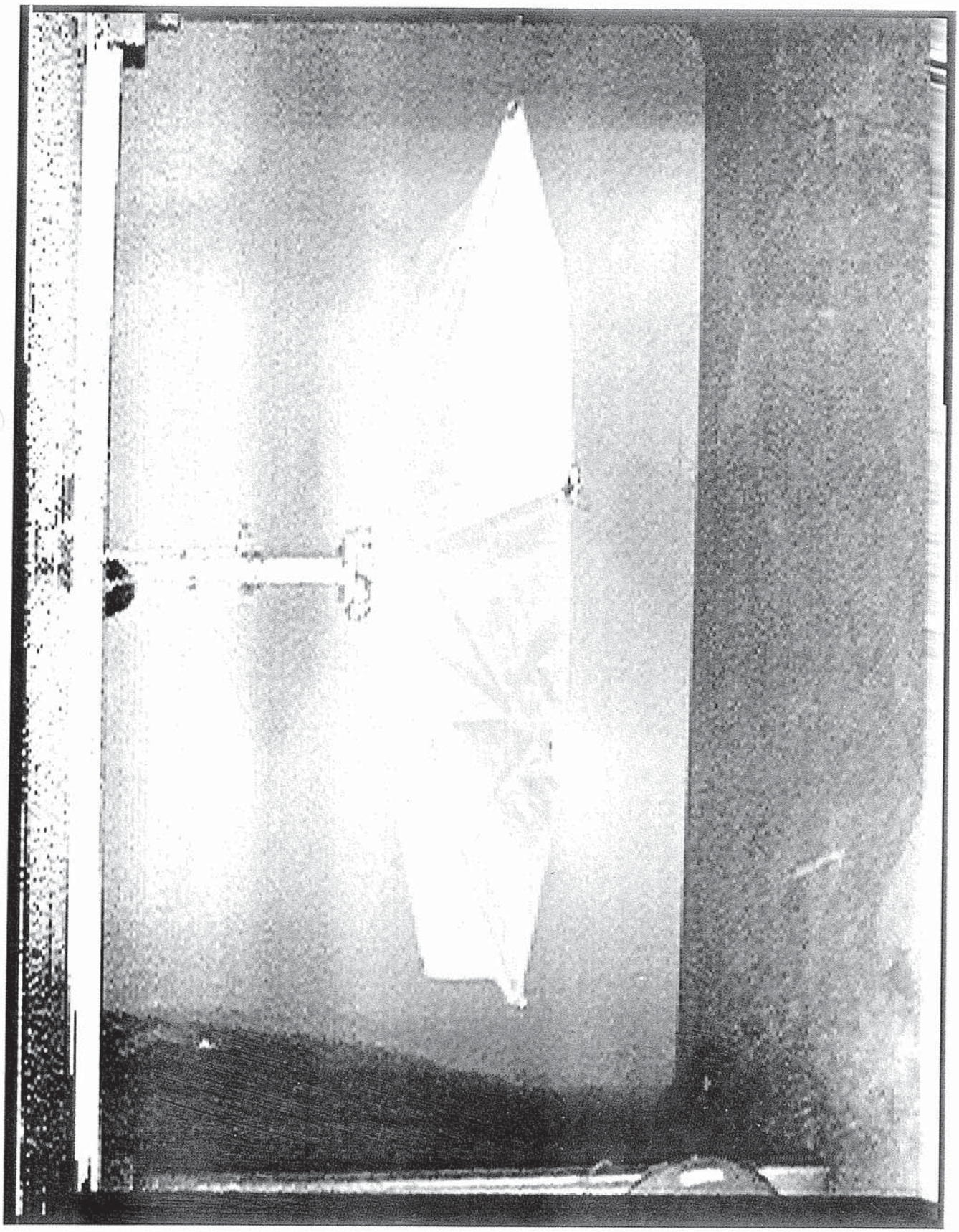

Fully-deployed model.

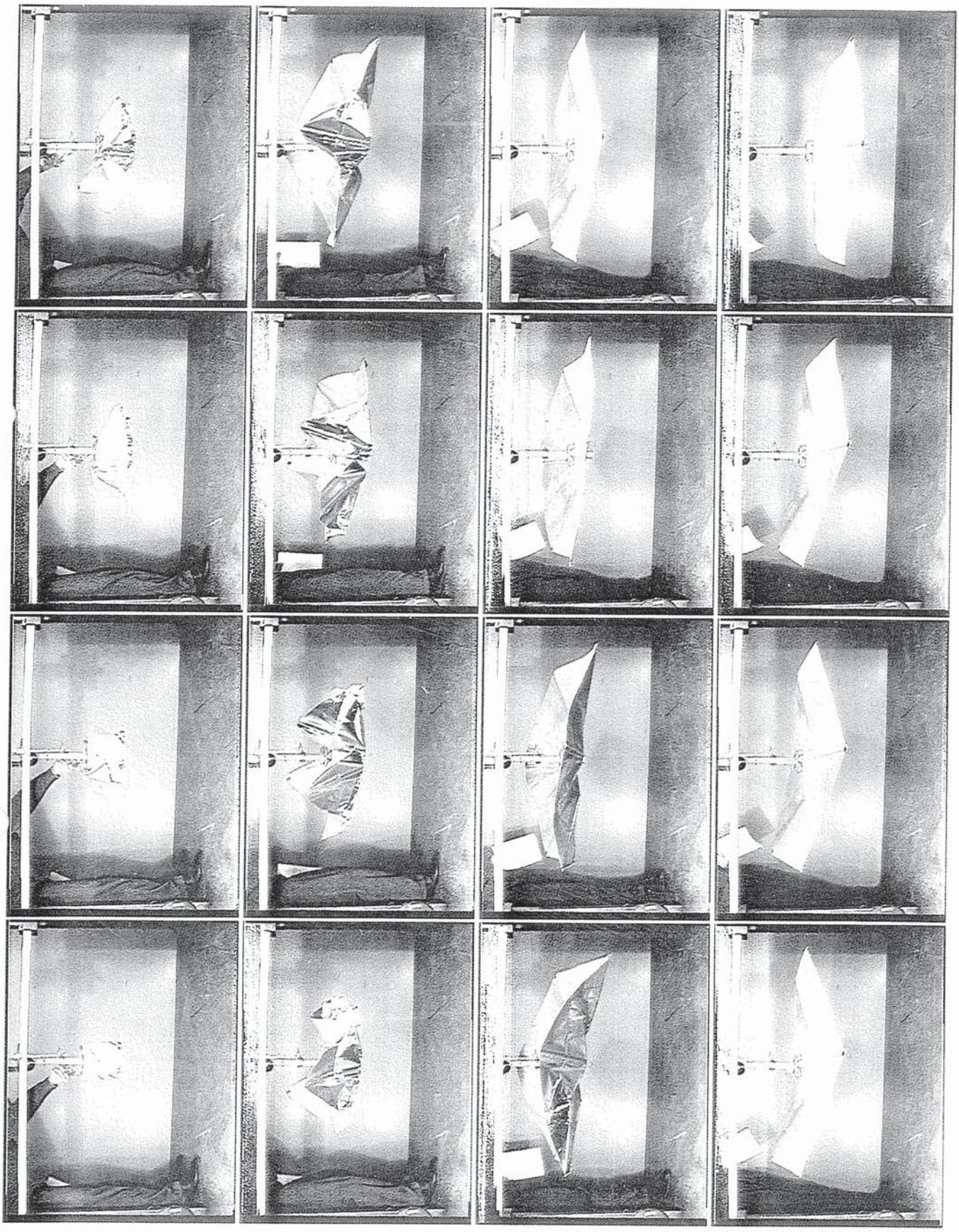

Deployment sequence 1.

Deployment sequence 2.

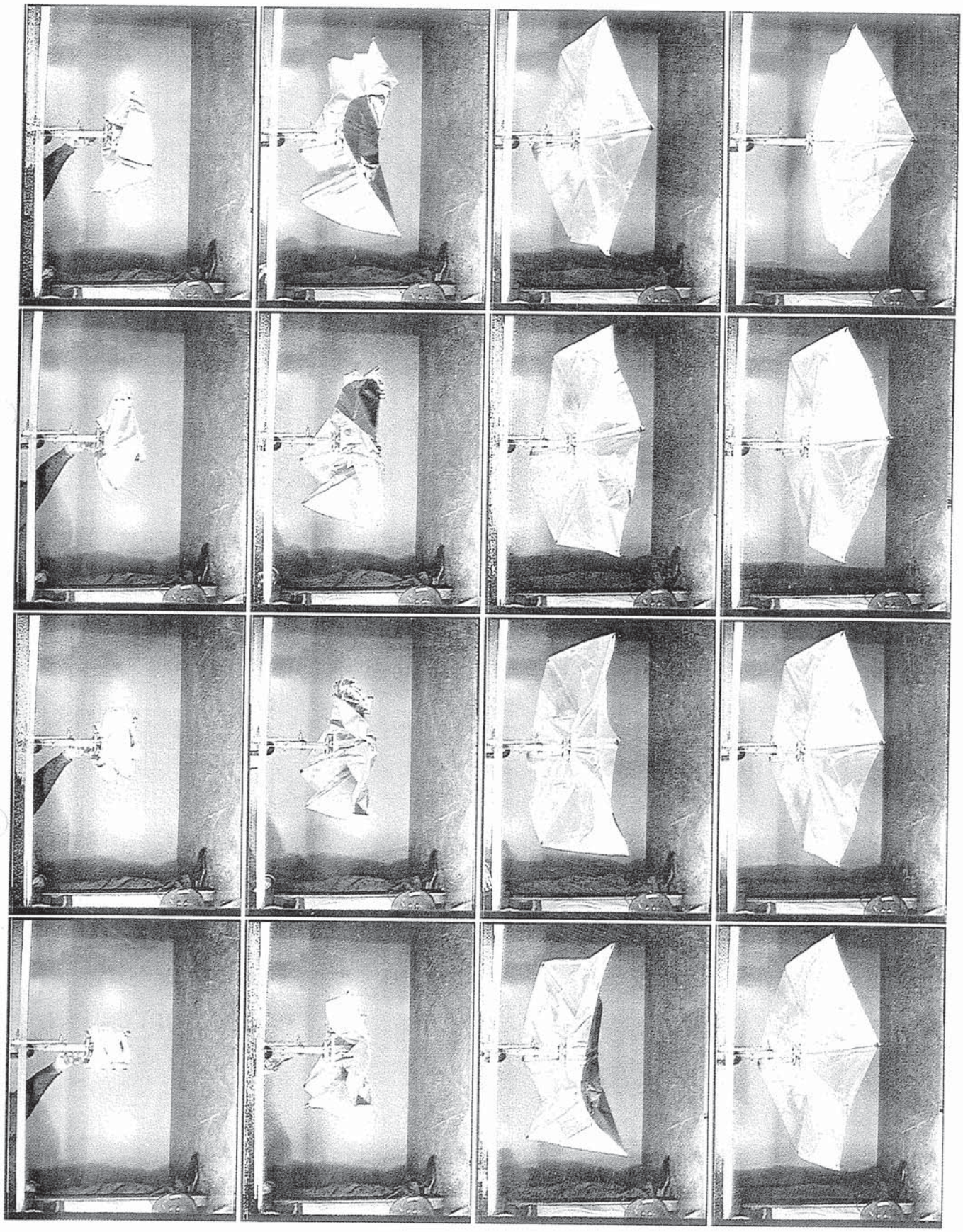

Deployment sequence 3.

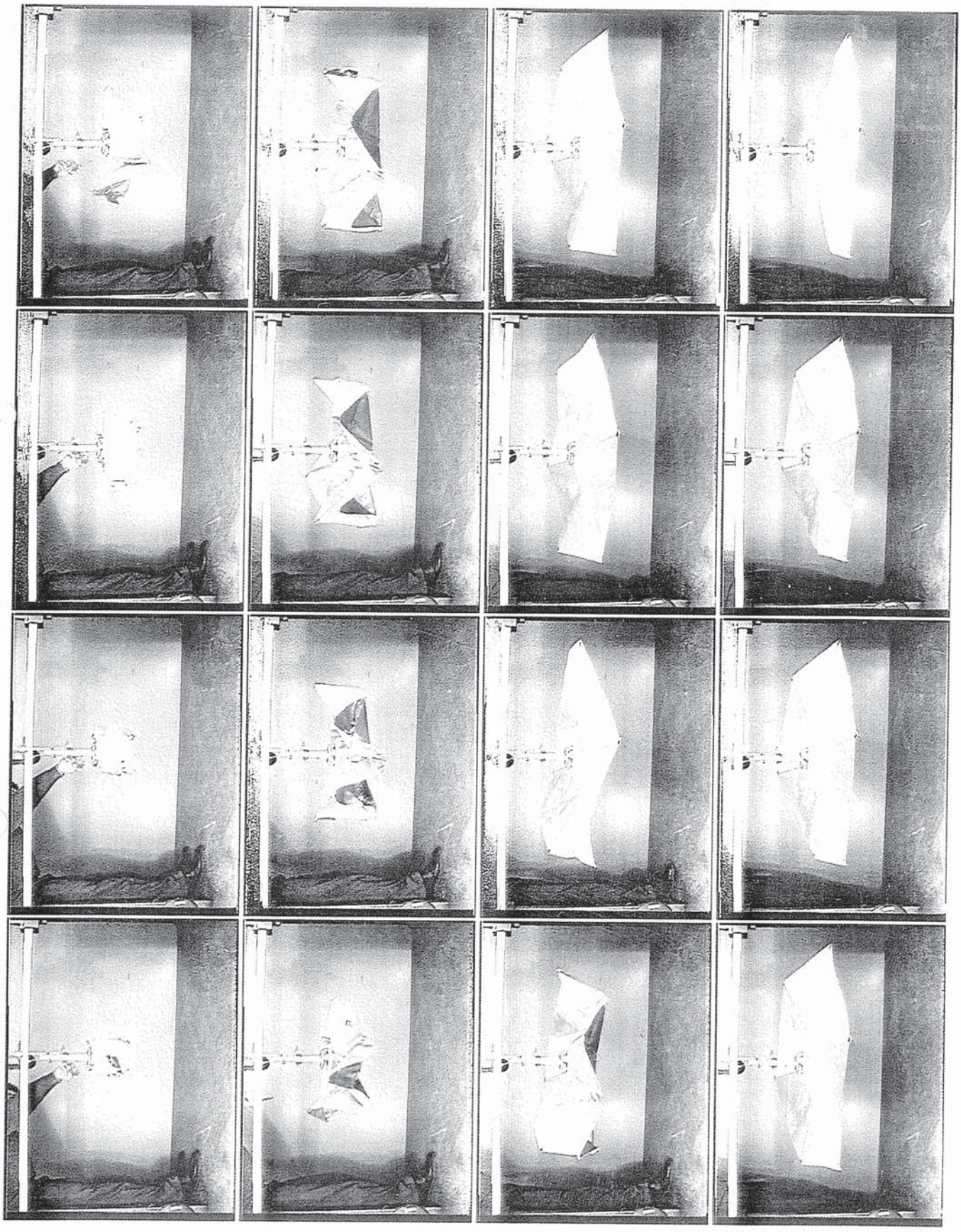

Deployment sequence 4.

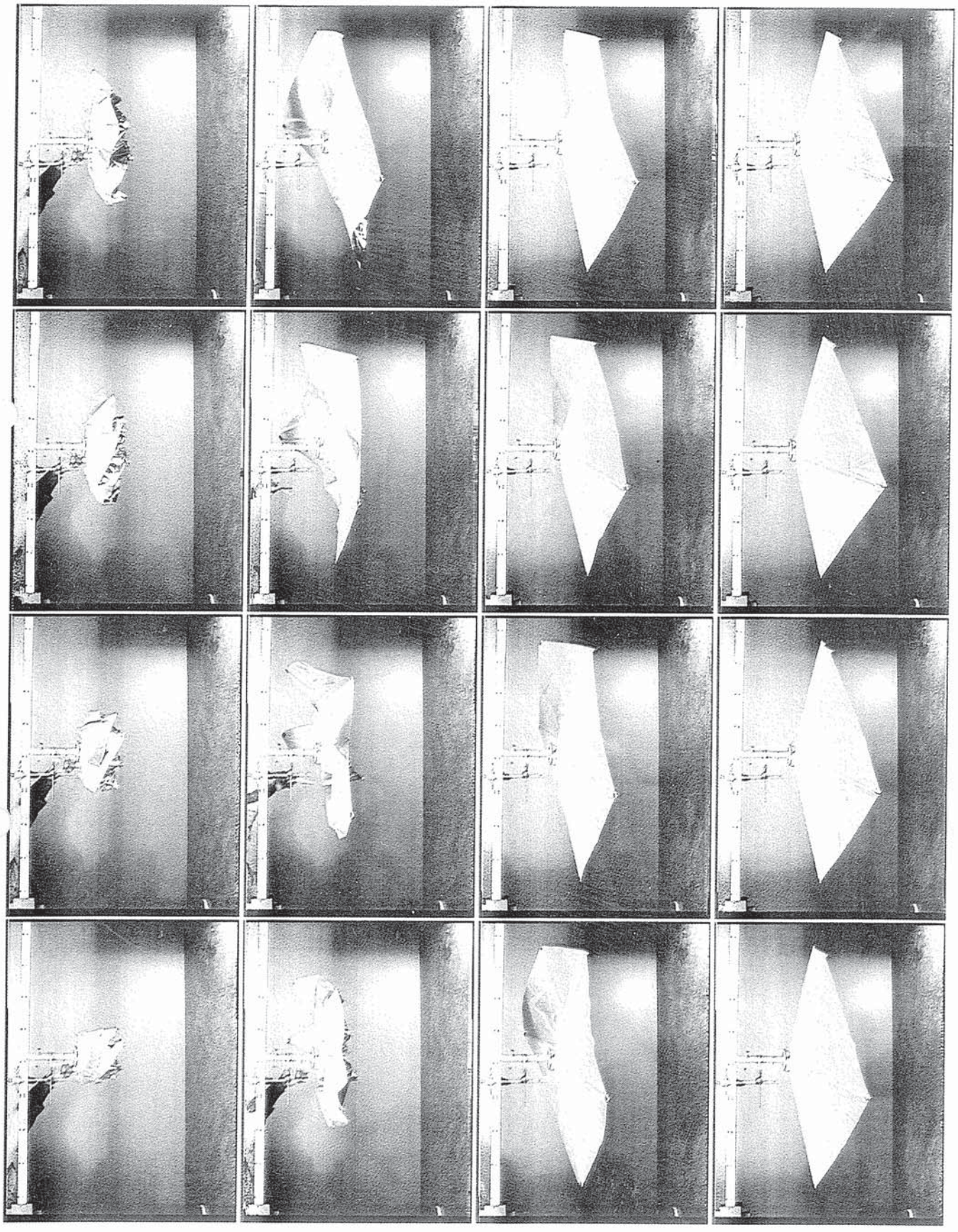

Deployment sequence 5.